Numerical simulation of an asymptotically reduced system for rotationally constrained convection

By MICHAEL SPRAGUE[1,2], KEITH JULIEN[1],
EDGAR KNOBLOCH[3] AND JOSEPH WERNE[4]

[1]Department of Applied Mathematics, University of Colorado, Boulder, CO 80309, USA

[2]School of Natural Sciences, University of California, Merced, CA 95344, USA

[3]Department of Physics, University of California, Berkeley, CA 94720, USA

[4]Colorado Research Associates Div., Northwest Research Associates, Boulder, CO 80301, USA

For rotationally constrained convection, the Taylor–Proudman theorem enforces an organization of nonlinear flows into tall columnar or compact plume structures. While coherent structures in convection under moderate rotation are exclusively cyclonic, recent experiments for rapid rotation have revealed a transition to equal populations of cyclonic and anticyclonic structures. Direct numerical simulation (DNS) of this regime is expensive, however, and existing simulations have yet to reveal anticyclonic vortical structures. In this paper, we use a reduced system of equations for rotationally constrained convection valid in the asymptotic limit of thin columnar structures and rapid rotation to perform numerical simulation of Rayleigh–Bénard convection in an infinite layer rotating uniformly about the vertical axis. Visualization indicates the existence of cyclonic and anticyclonic vortical populations for all parameters examined. Moreover, it is found that the flow evolves through three distinct regimes with increasing Rayleigh number (Ra). For small, but supercritical Ra, the flow is dominated by a cellular system of hot and cold columns spanning the fluid layer. As Ra increases, the number density of these columns decreases, the up- and down-drafts within them strengthen and the columns develop opposite-signed 'sleeves' in all fields. The resulting columns are highly efficient at transporting heat across the fluid layer. In the final regime, lateral mixing plays a dominant role in the interior and the columnar structure is destroyed. However, thermal plumes are still injected and rejected from the thermal boundary layers. We identify the latter two regimes with the vortex-grid and geostrophic turbulence regimes, respectively. Within these regimes, we investigate convective heat transport (measured by the Nusselt number), mean temperature profiles, and root-mean-square profiles of the temperature, vertical velocity and vertical vorticity anomalies. For all Prandtl numbers investigated, the mean temperature saturates in a non-isothermal profile as Ra increases owing to intense lateral mixing.

1. Introduction

In many objects of astrophysical and geophysical interest, thermal convection is strongly influenced by rotation. For instance, stars like our Sun possess a deep, turbulent, differentially rotating outer layer (Svestka & Harvey 2000). Deep outer

convection zones are also found on the giant planets (e.g. Jupiter, Saturn and Neptune) (Hubbard, Burrows & Lunine 2000), while convection within the Earth's interior plays an integral part in the geodynamo (Proctor & Gilbert 1994). Closer to home, open-ocean deep convection (Marshall & Schott 1999) represents a phenomenon with important contributions (such as water mass transformation) to the thermohaline circulation, i.e. the global overturning of the ocean on a thousand-year time scale. Here, vigorous localized downwellings are observed in high-latitude oceans, preconditioned by large-scale seasonal cooling and instigated by intense, but intermittent, local cooling events. In all these examples, the convective Rossby number Ro_{conv} is moderate to low, indicating that these flows are affected by rotation, while the Reynolds number Re (equivalently, the thermal Rayleigh number Ra) is high, implying that the flow is turbulent. Ro_{conv} is the ratio of rotation period to buoyancy free-fall time, and is a precise *a priori* measure of the importance of rotation.

Although much progress has been made in studying flows of this type, not only numerically and theoretically, but also experimentally, much remains to be learned about rotationally constrained turbulent motions (Proctor & Gilbert 1994; Marshall & Schott 1999; Svestka & Harvey 2000; Hubbard *et al.* 2000). The canonical example that retains the essence of these flows, where homogeneous forcing occurs over a large horizontal extent, is provided by rotating Rayleigh–Bénard convection, i.e. convection between two horizontal planes rotating rigidly about the vertical, with an imposed temperature difference across them. Early theoretical work on a horizontally unbounded layer showed that rotation delays the onset of convection (Chandrasekhar 1953, 1961), while subsequent work studied the development and saturation of the instability in the weakly nonlinear regime (Veronis 1968; Clune & Knobloch 1993 and references therein). The most notable achievement of the theory was the discovery of the Küppers–Lortz instability of convection rolls (Küppers & Lortz 1969), an orientation-changing instability that sets in at onset provided the rotation is sufficiently fast. The existence of this instability is now well documented experimentally (Zhong, Ecke & Steinberg 1991, 1993; Ning & Ecke 1993; Boubnov & Golitsyn 1995) and theoretically (Swift 1984; Clune & Knobloch 1993). Parallel to these developments, experiments in a rotating cylinder (Nakagawa & Frenzen 1955; Rossby 1969) revealed that for high rotation rates, convection, in fact, sets in considerably earlier than predicted by the unbounded-layer theory, a finding explained by the subsequent identification and description of a class of unstable modes (the so-called wall modes) that are absent in the unbounded system (Zhong *et al.* 1993; Goldstein *et al.* 1993). These developments are reviewed by Knobloch (1998).

Beyond the weakly nonlinear regime, the subsequent evolution of the system is strongly influenced by the magnitude of Ro_{conv}. Experimental observations in the regime $0.2 \lesssim Ro_{conv} \lesssim 1$ (Vorobieff & Ecke 1998, 2002) and detailed direct numerical simulation (DNS) for $Ro_{conv} = 0.75$ (Julien *et al.* 1996b) have revealed a breakdown of the cellular roll states, favoured near onset, to a dynamical state dominated by *cyclonic* vortical structures. These take the form of moving columns spanning the layer depth or long-lived coherent plumes forming out of an unstable thermal boundary layer. Indeed, Julien *et al.* (1996b) have observed strong chaotic vortical interactions between the structures in the form of merger and annihilation events in the presence of strong horizontal shears. Such vortical interactions are responsible for substantial lateral mixing that sustains an unstable mean temperature gradient in the fluid interior. An unstable mean temperature gradient that increases with rotation rate has also been observed in experiments by Hart & Ohlsen (1999) for fixed $Ra = 2 \times 10^{11}$ and $0.08 \lesssim Ro_{conv} \lesssim 1.7$. These observations represent significant departures from

non-rotating Rayleigh–Bénard convection, where isothermal interiors are produced owing to dominant vertical mixing. However, despite these marked differences, some similarities do exist. Most prominent is the remarkable finding that similar heat transport laws are observed (Rossby 1969). In particular, so-called hard turbulence ($Nu \sim Ra^{2/7}$, where Nu is the Nusselt number) has been observed at sufficiently high Ra in the presence of no-slip boundaries (Julien *et al.* 1996*a*; Liu & Ecke 1997), while the classical transport law ($Nu \sim Ra^{1/3}$) is found only in the presence of stress-free boundaries (Julien *et al.* 1996*a*).

For smaller Rossby numbers ($Ro_{conv} \lesssim 0.2$), the flow visualization experiments of Vorobieff & Ecke (2002) identified a striking topological change in the dynamics of the vortices. In the strongly nonlinear and turbulent regimes, plume generation in the thermal boundary layer now results in a new population of anticyclonic plumes, in addition to the cyclonic population. These appear via the formation of vortical thermal columns of cylindrical form, with either hot or cold thermal anomalies. Further, Vorobieff & Ecke (2002) show that the distribution of cyclonic and anticyclonic coherent structures approaches a balance as $Ro_{conv} \rightarrow 0$. It is likely that these columns are in geostrophic balance (Boubnov & Golitsyn 1986, 1995; Sakai 1997), although no experimental velocity measurements have confirmed this. Despite this, we refer to these in the following as 'Taylor' columns and the corresponding regime as the geostrophic vortex regime, since it bears some similarity to stable-layer quasi-geostrophic dynamics (Pedlosky 1987; Salmon 1998). However, a detailed understanding of the formation and dynamics of the Taylor columns remains open. For instance, in the experiments of Sakai (1997) (for $0.08 \lesssim Ro_{conv} \lesssim 0.70$), both hot and cold Taylor column populations are present, and are in a state of constant chaotic motion, while in the experiments of Boubnov & Golitsyn (1995) and Zhong *et al.* (1991, 1993) only Taylor columns of one sign (cold) are realized; these are observed to 'solidify' into a stationary triangular lattice. Similar vortex lattices are found even at relatively small Reynolds (Rayleigh) numbers (Bajaj *et al.* 1998). At high Reynolds (Rayleigh) numbers, however, the Taylor columns lose integrity and give way to long-lived plumes that form out of the thermal boundary layers, but no longer extend across the depth of the layer. We refer to this regime as geostrophic turbulence.

The current understanding of this topological change is still incomplete. For experiments, the challenge resides primarily in the accurate acquisition of highly resolved velocity, temperature and vortical fields (two-dimensional slices or three-dimensional volumes), although Vorobieff & Ecke (2002) have made substantial progress in acquiring near-boundary velocity fields using particle image velocimetry (PIV) techniques. For numerical simulations, the challenge resides in temporal and spatial resolution constraints imposed by prohibitively fast inertial waves and thin Ekman boundary layers. It is evident therefore that reduced equations in which fast inertial waves are filtered out and thin Ekman boundary layers are absent would be of great utility. This type of approach has been notably successful in the quasi-geostrophic regime (Pedlosky 1987; Salmon 1998), and has led to sophisticated balanced theories for stably stratified flows. Julien *et al.* (2006) established a firm connection of these theories to the unstably stratified case of interest here.

This paper focuses on a detailed numerical investigation of the high Re (high Ra) solutions to a set of reduced partial differential equations (PDEs) valid in the $Ro_{conv} \ll 1$ limit, and combines the approach of Julien *et al.* (2006) with the initial low Ra numerical investigation of Julien, Knobloch & Werne (1998). Major findings include the identification of three distinct flow regimes, all present for $Ro_{conv} \ll 1$ and

all involving vortical structures of both cyclonicities, including regimes we identify with the observed geostrophic vortex and geostrophic turbulence regimes. However, since the reduced equations are valid for $Ro_{conv} \ll 1$ only, the topological transition with increasing Ro_{conv} to a vortex population of one sign is absent.

The outline of this paper is as follows. In §2, a derivation of the reduced PDEs is given for the upright case (i.e. rotation anti-parallel to gravity). Some basic properties of the linear theory are then summarized, followed by a brief discussion of recently identified exact nonlinear single-mode solutions to the reduced PDEs. After a description of our numerical approach, a detailed discussion is given of the results obtained at various Prandtl numbers Pr corresponding to fluids ranging from air through water to high-viscosity fluids (i.e. $1 \leqslant Pr < \infty$). However, a detailed investigation of the statistical properties of the different regimes, including energy spectra, is postponed to a future publication. The paper concludes with a discussion of the implications of the results.

2. Derivation of the reduced model

We consider flow that is characterized by dimensional length, velocity, pressure and temperature scales L, U, $\widetilde{P}$ and $\widetilde{T}$, respectively, and adopt a Cartesian coordinate system $\boldsymbol{x} = (x, y, z)^T$ rotating with angular velocity $\boldsymbol{\Omega}$ about the z-axis, with gravity $\boldsymbol{g} = -g\widehat{\boldsymbol{z}}$. With these scales, the dimensionless Boussinesq equations governing the system are

$$\mathrm{D}_t \boldsymbol{u} + \frac{1}{Ro}\widehat{\boldsymbol{z}} \times \boldsymbol{u} = -P\nabla p + \Gamma\theta\widehat{\boldsymbol{z}} + \frac{1}{Re}\nabla^2 \boldsymbol{u}, \quad (2.1a)$$

$$\mathrm{D}_t\theta = \frac{1}{Pe}\nabla^2\theta, \quad (2.1b)$$

$$\nabla \cdot \boldsymbol{u} = 0, \quad (2.1c)$$

where $\boldsymbol{u} = (u, v, w)^T$ is the velocity, $\mathrm{D}_t \equiv \partial_t + \boldsymbol{u} \cdot \nabla$, p is the pressure, θ is the temperature, $Ro \equiv U/2\Omega L$ is the Rossby number, $P \equiv \widetilde{P}/\rho_0 U^2$ is the Euler number, $Pe \equiv UL/\kappa$ is the Péclet number, $Re \equiv UL/\nu$ is the Reynolds number, and $\Gamma \equiv -g\alpha\widetilde{T}L/U^2$ is the buoyancy number. Here, $\Omega = |\boldsymbol{\Omega}|$, α is the coefficient of thermal expansion, ρ_0 is a reference fluid density, ν is the kinematic viscosity and κ is the thermal diffusivity. We restrict the flow to an unbounded layer of fluid between two impenetrable rigid horizontal lids. Physically relevant boundary conditions include stress-free and/or no-slip mechanical boundary conditions, together with fixed temperature or fixed flux thermal boundary conditions or combinations thereof. In addition, we assume that the rotational Froude number $Fr_\Omega \equiv \Omega^2 L/g \ll 1$, so that the centrifugal buoyancy force is negligible compared to the gravitational buoyancy force. Neglect of the centrifugal buoyancy force $\Gamma Fr_\Omega\widehat{\boldsymbol{z}} \times \widehat{\boldsymbol{z}} \times \boldsymbol{x}$ in the momentum balance requires $\Gamma Fr_\Omega \ll 1$, a constraint that is assumed throughout this paper.

The above non-dimensionalization is generic in that precise velocity, length and time scales have not, as yet, been identified. Indeed, once the problem of interest is formulated, the system (2.1) can readily be recast into forms pertaining to various canonical problems in fluid mechanics. For example, in (slowly) rotating Rayleigh–Bénard convection in a plane unbounded fluid layer of depth H with temperature difference $\Delta\widetilde{T}$ imposed across it, it is customary to employ the choice $L \equiv H$ as the dimensional length scale, $U \equiv \nu/H$ as the dimensional velocity scale, H^2/ν as the

dimensional time scale, and set $\widetilde{T} = \Delta\widetilde{T}$. With these choices,

$$Ro = E, \quad |\Gamma| = \frac{Ra}{Pr}, \quad Re = 1, \quad Pe = Pr,$$

where $E \equiv \nu/2\Omega H^2$ is the Ekman number, $Ra \equiv g\alpha\Delta\widetilde{T}H^3/\nu\kappa$ is the Rayleigh number, and $Pr \equiv \nu/\kappa$ is the Prandtl number. In the rapidly rotating regime, this choice is not optimal, however, since such rotation reduces the horizontal scale of the flow, and it is this scale that becomes the natural scale. Consequently, we take L to be the horizontal scale, and, until we make a specific choice, work with the more general non-dimensionalization (2.1).

2.1. *Asymptotic theory for $Ro \ll 1$ and $A_Z \gg 1$*

The Taylor–Proudman (Proudman 1916; Taylor 1923) constraint suggests that rapidly rotating convection takes place in tall columnar structures. Consequently we characterize the flow by its aspect ratio $A_Z := H/L$, where H is the depth of the fluid layer and L is the characteristic scale in the horizontal. For tall columnar structures, $A_Z \gg 1$. In addition to a small vertical scale z, we introduce a large scale, $Z := A_Z^{-1}z$, over which the columns are modulated. A multiple time scale expansion is also required. We suppose, following Julien *et al.* (1998, 2005), that $T := A_T^{-1}t$, $A_T \gg 1$, is a slow time, and employ the substitutions

$$\partial_z \to \partial_z + \frac{1}{A_Z}\partial_Z, \quad \partial_t \to \partial_t + \frac{1}{A_T}\partial_T. \tag{2.2}$$

These result in the rescaled equations

$$\left(D_t + \frac{1}{A_T}\partial_T + \frac{w}{A_Z}\partial_Z\right)\boldsymbol{u} + \frac{1}{Ro}\widehat{\boldsymbol{z}}\times\boldsymbol{u} = -P\left(\nabla + \frac{\widehat{\boldsymbol{z}}}{A_Z}\partial_Z\right)p + \Gamma\theta\widehat{\boldsymbol{z}}$$
$$+ \frac{1}{Re}\left(\nabla + \frac{\widehat{\boldsymbol{z}}}{A_Z}\partial_Z\right)^2\boldsymbol{u}, \tag{2.3a}$$

$$\left(D_t + \frac{1}{A_T}\partial_T + \frac{w}{A_Z}\partial_Z\right)\theta = \frac{1}{Pe}\left(\nabla + \frac{\widehat{\boldsymbol{z}}}{A_Z}\partial_Z\right)^2\theta, \tag{2.3b}$$

$$\nabla\cdot\boldsymbol{u} + \frac{1}{A_Z}\partial_Z w = 0. \tag{2.3c}$$

We now use these equations to derive a closed set of reduced equations.

We begin by averaging equations (2.3) over fast temporal and small spatial scales, obtaining

$$\frac{1}{A_T}\partial_T\overline{\boldsymbol{u}} + \frac{1}{A_Z}\partial_Z\left(\overline{w\boldsymbol{u}}\right) + \frac{1}{Ro}\widehat{\boldsymbol{z}}\times\overline{\boldsymbol{u}} = \left(-\frac{P}{A_Z}\partial_Z\overline{p} + \Gamma\overline{\theta}\right)\widehat{\boldsymbol{z}} + \frac{1}{ReA_Z^2}\partial_Z^2\overline{\boldsymbol{u}}, \tag{2.4a}$$

$$\frac{1}{A_T}\partial_T\overline{\theta} + \frac{1}{A_Z}\partial_Z(\overline{w\theta}) = \frac{1}{PeA_Z^2}\partial_Z^2\overline{\theta}, \tag{2.4b}$$

$$\partial_Z\overline{w} = 0, \tag{2.4c}$$

where the overbar denotes the operation

$$\overline{f}(Z,T) := \lim_{\tau,V\to\infty}\frac{1}{\tau V}\int_{\tau,V} f(\boldsymbol{x},Z,t,T)\,\mathrm{d}\boldsymbol{x}\,\mathrm{d}t, \tag{2.5}$$

for any dependent quantity f. To obtain these equations we used the vector identity $\boldsymbol{u}\cdot\nabla\gamma = \nabla\cdot(\gamma\boldsymbol{u}) - \gamma\nabla\cdot\boldsymbol{u}$, where γ is a scalar.

To obtain equations for fluctuating quantities, we write the dependent variables $\boldsymbol{v} = (\boldsymbol{u}, p, \theta)^T$ in (2.3) as a sum of their mean and fluctuating components, i.e.

$$\boldsymbol{v}(\boldsymbol{x}, Z, t, T) = \overline{\boldsymbol{v}}(Z, T) + \boldsymbol{v}'(\boldsymbol{x}, Z, t, T), \tag{2.6}$$

and subtract the associated mean equations (2.4):

$$\left(\mathrm{D}_t + \frac{1}{A_T} \partial_T + \frac{w}{A_Z} \partial_Z \right) \boldsymbol{u}' + \frac{w'}{A_Z} \partial_Z \overline{\boldsymbol{u}} - \frac{1}{A_Z} \partial_Z (\overline{w' \boldsymbol{u}'}) + \frac{1}{Ro} \widehat{\boldsymbol{z}} \times \boldsymbol{u}'$$
$$= -P \left(\nabla + \frac{\widehat{\boldsymbol{z}}}{A_Z} \partial_Z \right) p' + \Gamma \theta' \widehat{\boldsymbol{z}} + \frac{1}{Re} \left(\nabla + \frac{\widehat{\boldsymbol{z}}}{A_Z} \partial_Z \right)^2 \boldsymbol{u}', \tag{2.7a}$$

$$\left(\mathrm{D}_t + \frac{1}{A_T} \partial_T + \frac{w}{A_Z} \partial_Z \right) \theta' + \frac{w'}{A_Z} \partial_Z \overline{\theta} - \frac{1}{A_Z} \partial_Z (\overline{w' \theta'}) = \frac{1}{Pe} \left(\nabla + \frac{\widehat{\boldsymbol{z}}}{A_Z} \partial_Z \right)^2 \theta', \tag{2.7b}$$

$$\nabla \cdot \boldsymbol{u}' + \frac{1}{A_Z} \partial_Z w' = 0. \tag{2.7c}$$

Next, we expand the dependent variables $\boldsymbol{v} = (\overline{\boldsymbol{u}}, \boldsymbol{u}', \overline{p}, p', \overline{\theta}, \theta')^T$ in terms of the small parameter $Ro \equiv \epsilon$,

$$\boldsymbol{v} = \boldsymbol{v}_0 + \epsilon \boldsymbol{v}_1 + \epsilon^2 \boldsymbol{v}_2 + O(\epsilon^3), \tag{2.8}$$

and, following Julien *et al.* (2005), choose the scalings

$$A_Z = \epsilon^{-1}, \quad A_T = \epsilon^{-2}, \quad \Gamma = \epsilon^{-1} \widetilde{\Gamma}, \tag{2.9}$$

where $\widetilde{\Gamma}$, like Re and Pe, is of order one. Examination of the vertical component of equation (2.4a) now reveals that for hydrostatic balance at leading order we must take $P = \epsilon^{-2}$. Thus,

$$\partial_Z \overline{p}_0 = \widetilde{\Gamma} \overline{\theta}_0. \tag{2.10}$$

Moreover, the leading-order horizontal components then imply that $\overline{\boldsymbol{u}}_{0\perp} \equiv (\overline{u}_0, \overline{v}_0, 0)^T = \boldsymbol{0}$. Since equation (2.4c) implies that $\overline{w} \equiv 0$, it follows that $\overline{\boldsymbol{u}}_0 \equiv \boldsymbol{0}$, resulting in a substantial simplification.

At $O(1)$, the mean buoyancy equation now gives

$$\partial_Z (\overline{w_0' \theta_0'}) = 0,$$

implying that $\overline{w_0' \theta_0'} = 0$, a condition that is in general satisfied only when $w_0' \equiv 0$ or $\theta_0' \equiv 0$. The former is unphysical in that it requires the small-scale, rotationally constrained flow to be hydrostatic. Therefore, in the following, we take $\theta_0' \equiv 0$, implying that buoyancy fluctuations about the mean temperature profile $\overline{\theta}_0(Z)$ are $O(\epsilon)$.

At $O(\epsilon)$ the mean and fluctuating buoyancy equations give

$$\partial_T \overline{\theta}_0 + \partial_Z (\overline{w_0' \theta_1'}) = \frac{1}{Pe} \partial_Z^2 \overline{\theta}_0, \tag{2.11}$$

and

$$\mathrm{D}_t^0 \theta_1' + w_0' \partial_Z \overline{\theta}_0 = \frac{1}{Pe} \nabla^2 \theta_1', \tag{2.12}$$

respectively, where $\mathrm{D}_t^0 \equiv \partial_t + \boldsymbol{u}_0' \cdot \nabla$ and we have used the fact that $\theta_0' = 0$. At $O(\epsilon^{-2})$, the momentum equation yields

$$\nabla p_0' = \boldsymbol{0}, \tag{2.13}$$

implying that $p'_0 = 0$. With $\theta'_0 = p'_0 = 0$, the momentum equation at $O(\epsilon^{-1})$ and $O(1)$ now yields

$$\widehat{z} \times \boldsymbol{u}'_0 = -\nabla p'_1, \tag{2.14}$$

$$\mathrm{D}_t^0 \boldsymbol{u}'_0 + \widehat{z} \times \boldsymbol{u}'_1 = -\nabla p'_2 + (-\partial_Z p'_1 + \widetilde{\Gamma} \theta'_1) \widehat{z} + \frac{1}{Re} \nabla^2 \boldsymbol{u}'_0. \tag{2.15}$$

Finally, the continuity equation at $O(1)$ and $O(\epsilon)$ yields

$$\nabla \cdot \boldsymbol{u}'_0 = 0, \tag{2.16}$$

$$\nabla \cdot \boldsymbol{u}'_1 + \partial_Z w'_0 = 0. \tag{2.17}$$

The system of equations (2.10)–(2.12), (2.14)–(2.17) is closed, but still quite involved. However, owing to its special structure, it is amenable to further simplification, as described next.

2.2. *The Taylor–Proudman constraint and the dynamics of the reduced system*

Equation (2.14) indicates that the leading-order flow is in geostrophic balance. Moreover, the curl of this equation implies both that $\widehat{z} \cdot \nabla \boldsymbol{u}'_{0\perp} = \boldsymbol{0}$ and $\nabla_\perp \cdot \boldsymbol{u}'_{0\perp} = 0$ (i.e. the horizontal flow is non-divergent on small scales). Here, $\nabla_\perp \equiv (\partial_x, \partial_y, 0)^T$. Since (2.16) then implies that $\partial_z w'_0 = 0$, it follows that

$$(\widehat{z} \cdot \nabla) \boldsymbol{u}'_0 = \boldsymbol{0}. \tag{2.18}$$

Likewise, applying $\widehat{z} \cdot$ to (2.14) and $\widehat{z} \cdot \nabla$ to (2.12), we find that

$$(\widehat{z} \cdot \nabla) p'_1 = 0, \quad (\widehat{z} \cdot \nabla) \theta'_1 = 0. \tag{2.19}$$

These three relations express the Taylor–Proudman constraint that forces leading-order motion on small spatial scales to be invariant in the direction of the rotation axis. It follows that $\boldsymbol{u}'_0$, p'_1, θ'_1 depend on height through the slow variable Z only. This is not so automatic for the higher-order terms. However, if we interpret the vertical component of equation (2.15) as an equation for p'_2, we see immediately that p'_2 will grow secularly with the small-scale variable z, unless the remaining terms balance. Thus, we require the *solvability* condition

$$\mathrm{D}_t^0 w'_0 + \partial_Z p'_1 = \widetilde{\Gamma} \theta' + \frac{1}{Re} \nabla_\perp^2 w'_0. \tag{2.20}$$

The horizontal components likewise yield an equation for w'_1, and the corresponding solvability condition is

$$\mathrm{D}_t^0 (\widehat{z} \cdot \nabla \times \boldsymbol{u}'_0) = \partial_Z w'_0 + \frac{1}{Re} \nabla_\perp^2 (\widehat{z} \cdot \nabla \times \boldsymbol{u}'_0). \tag{2.21}$$

These solvability conditions, together with equations (2.11), (2.12) and (2.16), represent the desired reduced system of equations, and guarantee that p'_2 and w'_1 satisfy the Taylor–Proudman constraint as well.

It is instructive at this stage to highlight the differences between geostrophy in the classical small-aspect-ratio regime (Pedlosky 1987; Salmon 1998) and the present large-aspect-ratio case. In both cases, geostrophy implies horizontally non-divergent leading-order flow, $\nabla_\perp \cdot \boldsymbol{u}'_{0\perp} = 0$, and consequently that $\partial_z w'_0 = 0$. However, in the small-aspect-ratio regime, the strong stable stratification permits weak vertical motions only, i.e. $w'_0 = 0$, while in the present large-aspect-ratio case, the unstable stratification permits substantial vertical motions, i.e. $w'_0 \neq 0$. These, in turn, demand weakly divergent horizontal motions at next order, as described by equation (2.17). These considerations do not arise in classical geostrophy.

2.3. Streamfunction formulation

In order to satisfy the continuity conditions (2.16), (2.17) automatically, we use a streamfunction formulation defined by

$$\boldsymbol{u}' = -\nabla \times \psi \hat{\boldsymbol{z}} - \nabla \times \nabla \times \phi \hat{\boldsymbol{z}}. \qquad (2.22)$$

Since $\boldsymbol{u}_0'$ is independent of the small-scale z it follows that

$$\boldsymbol{u}_0' = (-\partial_y \psi_0, \ \partial_x \psi_0, \ \nabla_\perp^2 \phi_0)^T, \qquad (2.23a)$$

$$\boldsymbol{u}_1' = (-\partial_{xZ}^2 \phi_0, \ -\partial_{yZ}^2 \phi_0, \ 0)^T + (-\partial_y \psi_1, \ \partial_x \psi_1, \ \nabla_\perp^2 \phi_1)^T. \qquad (2.23b)$$

From (2.14), it now follows that $p_1' = \psi_0$, and equations (2.20), (2.21), (2.12) and (2.11) become

$$\partial_t \nabla_\perp^2 \phi + J(\psi, \nabla_\perp^2 \phi) + \partial_Z \psi = \widetilde{\Gamma} \theta' + Re^{-1} \nabla_\perp^4 \phi, \qquad (2.24a)$$

$$\partial_t \nabla_\perp^2 \psi + J(\psi, \nabla_\perp^2 \psi) - \partial_Z \nabla_\perp^2 \phi = Re^{-1} \nabla_\perp^4 \psi, \qquad (2.24b)$$

$$\partial_t \theta' + J(\psi, \theta') + \nabla_\perp^2 \phi \partial_Z \overline{\theta} = Pe^{-1} \nabla_\perp^2 \theta', \qquad (2.24c)$$

$$\partial_T \overline{\theta} + \partial_Z (\overline{\theta' \nabla_\perp^2 \phi}) = Pe^{-1} \partial_Z^2 \overline{\theta}, \qquad (2.24d)$$

where $J(f, g) := \partial_x f \partial_y g - \partial_x g \partial_y f$ and the subscripts on ψ_0, ϕ_0, θ_1' and $\overline{\theta}_0$ denoting the asymptotic order have been dropped. Note that the coupling between ψ and ϕ occurs through the slow variable Z via stretching due to the Coriolis force. The nonlinearities in the momentum equations (2.24a, b) arise solely through horizontal advection. We also remark on the absence of vertical diffusion of the fluctuating quantities, a geometric consequence of the assumption $A_Z \gg 1$. This reduction in the order of the system in the vertical relegates boundary-layer effects to higher order and renders them passive (Julien & Knobloch 1998). Consequently, we need only employ impenetrable boundary conditions on the upper and lower surfaces together with appropriate temperature boundary conditions. When the boundary conditions are no-slip, the velocity boundary layer is of depth $\lambda \sim O(Ro^{3/2} Re^{-1/2})$ relative to H, and its structure can be deduced from the instantaneous interior solution.

Equations (2.24) possess an unexpected reflection symmetry

$$(x, y) \to (x, -y), \quad (\psi, \phi, \theta', \overline{\theta}) \to (-\psi, -\phi, -\theta', \overline{\theta}), \qquad (2.25)$$

that is absent in the original equations (2.1). This extra symmetry is a consequence of the absence of pseudoscalar terms in (2.24), and its consequences are profound: at leading order, rotationally constrained flows with $Ro \ll 1$ have the same symmetry properties as non-rotating flows (Julien & Knobloch 1999), even though at finite Ro this is no longer so; the horizontal velocity components $\boldsymbol{u}_\perp' \approx \boldsymbol{u}_{0\perp}' + Ro \, \boldsymbol{u}_{1\perp}'$ in (2.23) do not share this symmetry. The full flow does, therefore, manifest the handedness expected of a rotating system and present in the Navier–Stokes equations in primitive variables. However, the presence of this asymptotic symmetry has important consequences for the types of solutions admitted by these equations and their stability. In particular, in the limit $Ro \ll 1$ the Küppers–Lortz instability is suppressed, and the preference for cyclonic coherent structure disappears.

2.4. Rotating Rayleigh–Bénard convection

Equations (2.24) represent the generic reduced equations. If we choose $U \equiv \nu/L$ as the velocity scale for viscous diffusion in the horizontal and L^2/ν for the corresponding

time scale, then

$$Re \equiv 1, \quad Pe \equiv Pr, \quad \widetilde{\Gamma} \equiv \frac{\epsilon Ra}{Pr A_Z^3}, \quad Ro = A_Z^2 E = \epsilon, \quad A_Z = \epsilon^{-1}. \tag{2.26}$$

Thus, $E \equiv Ro^3 = \epsilon^3$ and $\widetilde{\Gamma} \equiv \epsilon^4 Ra/Pr$. We therefore introduce the scaled Rayleigh number $\widetilde{Ra} := \epsilon^4 Ra \equiv E^{4/3} Ra$, such that $\widetilde{\Gamma} = \widetilde{Ra}/Pr$ is of order one. These relations are consistent with linear theory for rapidly rotating convection (Chandrasekhar 1961). Moreover, one rotation period $2\pi/\Omega$ is equivalent to the non-dimensional time $4\pi E^{1/3}$. The rescaled equations are

$$\partial_t \nabla_\perp^2 \phi + J(\psi, \nabla_\perp^2 \phi) + \partial_Z \psi = \frac{\widetilde{Ra}}{Pr} \theta' + \nabla_\perp^4 \phi, \tag{2.27a}$$

$$\partial_t \nabla_\perp^2 \psi + J(\psi, \nabla_\perp^2 \psi) - \partial_Z \nabla_\perp^2 \phi = \nabla_\perp^4 \psi, \tag{2.27b}$$

$$\partial_t \theta' + J(\psi, \theta') + \nabla_\perp^2 \phi \partial_Z \overline{\theta} = Pr^{-1} \nabla_\perp^2 \theta', \tag{2.27c}$$

$$\partial_T \overline{\theta} + \partial_Z (\overline{\theta' \nabla_\perp^2 \phi}) = Pr^{-1} \partial_Z^2 \overline{\theta}, \tag{2.27d}$$

and are used in this form in our numerical simulations (modulo a small modification discussed in §3).

2.5. *Infinite Prandtl number*

Our investigations indicate that it is also of interest to consider rapidly rotating convection in the limit of infinite Prandtl number. For this problem, the appropriate time scale is the horizontal *thermal* diffusion time. With the substitutions

$$t \to Pr\, t, \quad T \to Pr\, T, \quad \psi \to \frac{\psi}{Pr}, \quad \phi \to \frac{\phi}{Pr}, \tag{2.28}$$

the system (2.27) becomes, in the limit $Pr \to \infty$,

$$\partial_Z \psi = \widetilde{Ra}\, \theta' + \nabla_\perp^4 \phi, \tag{2.29a}$$

$$-\partial_Z \nabla_\perp^2 \phi = \nabla_\perp^4 \psi, \tag{2.29b}$$

$$\partial_t \theta' + J(\psi, \theta') + \nabla_\perp^2 \phi \partial_Z \overline{\theta} = \nabla_\perp^2 \theta', \tag{2.29c}$$

$$\partial_T \overline{\theta} + \partial_Z (\overline{\theta' \nabla_\perp^2 \phi}) = \partial_Z^2 \overline{\theta}. \tag{2.29d}$$

In this system, the velocity field adjusts instantaneously to the thermal fluctuations.

2.6. *Boundary conditions*

In all the simulations that follow, we employ impenetrable fixed-temperature boundary conditions, i.e.

$$\phi|_{Z=0} = \phi|_{Z=1} \equiv 0, \quad \theta'|_{Z=0} = \theta'|_{Z=1} \equiv 0, \quad \overline{\theta}|_{Z=0} = 1, \quad \overline{\theta}|_{Z=1} = 0. \tag{2.30a–d}$$

The governing equations then give

$$\partial_Z \psi|_{Z=0} = \partial_Z \psi|_{Z=1} \equiv 0, \quad \partial_Z^2 \phi|_{Z=0} = \partial_Z^2 \phi|_{Z=1} \equiv 0, \tag{2.31a, b}$$

implying a natural association at leading order with stress-free boundary conditions. As noted earlier, other velocity boundary conditions lead to passive boundary layers (see, for instance, the $O(E^{1/2})$ Ekman boundary layer associated with no-slip boundaries), which can be computed *a posteriori* once the interior solution is known.
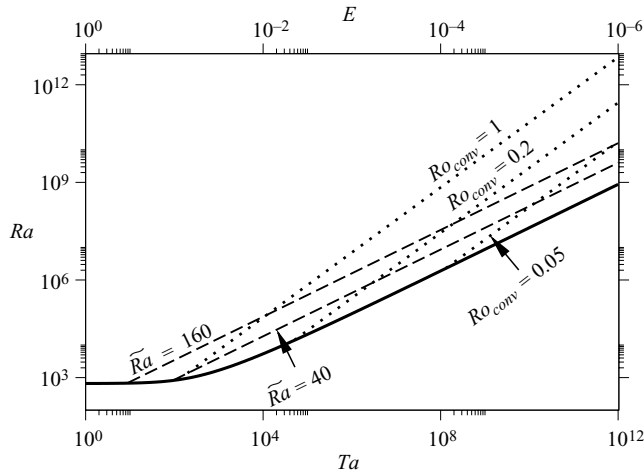
FIGURE 1. *Ra vs. Ta* parameter space demarcating (*i*) the critical Rayleigh number for onset of steady convection in the presence of fixed temperature and stress-free boundaries (solid line), (*ii*) lines of constant reduced Rayleigh number $E^{4/3}Ra$ (dashed lines), and (*iii*) lines of constant convective Rossby number Ro_{conv} (dotted lines), for $Pr = 7$.

2.7. *Linear stability results*

For the purpose of providing a basis for interpreting the results from our numerical simulations of the reduced equations (2.27), we briefly summarize the linear stability properties of the conduction state,

$$\psi = \phi = \theta' = 0, \quad \overline{\theta} = 1 - Z, \qquad (2.32)$$

for the reduced equations. These can also be deduced by taking the $Ro \equiv E^{1/3} \ll 1$ limit of the corresponding results obtained from the unscaled system by Chandrasekhar (1961). In this limit, the results become independent of the velocity boundary conditions at the top and bottom of the layer. We finds that for $Pr > Pr^* \approx 0.676605$ the conduction state loses stability to monotonically growing perturbations with horizontal wavenumber $\widetilde{k}$ at

$$\widetilde{Ra}^{(s)} = \widetilde{k}^4 + \frac{\pi^2}{\widetilde{k}^2}. \qquad (2.33)$$

The minimum value of $\widetilde{Ra}^{(s)}$ and the corresponding critical wavenumber are given by

$$\widetilde{Ra}_c^{(s)} = 3\left(\frac{\pi^2}{2}\right)^{2/3} \approx 8.6956, \quad \widetilde{k}_c^{(s)} = \left(\frac{\pi^2}{2}\right)^{1/6} \approx 1.3048. \qquad (2.34)$$

The critical wavelength is thus $L_c = 2\pi/\widetilde{k}_c^{(s)} \approx 4.8154$. The bifurcation to oscillations that are preferred for $Pr < Pr^*$ is not of interest in what follows.

In §4, we report on numerical simulation results in the range $\widetilde{Ra}_c^{(s)} \leqslant \widetilde{Ra} \leqslant 160$ of scaled Rayleigh numbers, and various values of $Pr \geqslant 1$. In the Rayleigh number (Ra) vs. Taylor number $(Ta \equiv E^{-2})$ parameter space (figure 1), lines of constant $\widetilde{Ra}$ correspond to lines of constant slope 2/3 above the onset of bulk convection (see the solid line and equation (2.34)). Also shown, for comparison with previous investigations (Boubnov & Golitsyn 1995; Julien *et al.* 1996*a,b*; Liu & Ecke 1997), are the (dotted) lines of constant convective Rossby number $Ro_{conv} = E\sqrt{Ra/Pr}$ for

$\widetilde{Ra}$	$Nu = -\partial_Z\overline{\theta}_0\vert_{Z=1}$	$-\partial_Z\overline{\theta}_0\vert_{Z=1/2}$	$\widetilde{Ra}$	$Nu = -\partial_Z\overline{\theta}_0\vert_{Z=1}$	$-\partial_Z\overline{\theta}_0\vert_{Z=1/2}$
8.6956	1.0000	1.0000	40	19.177	0.14933
10	1.3253	0.77356	80	59.291	0.07403
20	5.3583	0.31080	160	164.06	0.03693

TABLE 1. Mean temperature gradients at $Z=1$ and $Z=1/2$ deduced from the single mode solutions of Julien & Knobloch (1998, 1999).

$Pr = 7$, representing the ratio of the rotation period to buoyancy free-fall time. These have slope 1. As already mentioned, the convective Rossby number is a precise *a priori* measure of the importance of rotation as Ra is varied (Julien *et al.* 1996b), and remains small even when $Ra = E^{-4/3}\widetilde{Ra}$, namely, $Ro_{conv} = E^{1/3}\sqrt{\widetilde{Ra}/Pr}$. This observation leads to three important remarks concerning the interpretation of the simulation results that follow in §4. First, for $\widetilde{Ra} = O(1)$ the limit of small Rossby numbers is equivalent to the requirement $E^{1/3} \ll 1$; the numerical simulation results that follow apply to rotating convection only in this limit. Secondly, the range of supercritical Rayleigh numbers for which convection is strongly affected by rotation increases with rotation. Finally, for primary geostrophic balance we require that $Ro_{conv} \ll 1$, i.e. $E^{1/3}\sqrt{\widetilde{Ra}/Pr} \ll 1$, a constraint on the magnitude of the permitted $\widetilde{Ra}$ that is weaker than the formal requirement $\widetilde{Ra} = O(1)$. For comparison, for $Ro_{conv} \lesssim 0.2$ experiments of Sakai (1997), which span $8.6 \times 10^5 \lesssim Ra \lesssim 8.2 \times 10^7$, $9.1 \times 10^5 \lesssim Ta \lesssim 1.1 \times 10^9$, and those of Vorobieff & Ecke (2002), which span $0 \leqslant Ta \lesssim 10^{10}$ at $Ra = 3.2 \times 10^8$, correspond to $23 \lesssim \widetilde{Ra} \lesssim 144$ and $\widetilde{Ra} \lesssim 171$ respectively.

2.8. *Single-mode solutions*

A remarkable feature of equations (2.27) is that they admit exact single-mode (i.e. single-wavenumber) nonlinear solutions in separable form $\phi = \Phi(Z)h(x, y)$, where $h(x, y)$ satisfies the *planform* equation

$$\nabla_\perp^2 h = -\widetilde{k}^2 h, \qquad \overline{h^2} = 1. \qquad (2.35)$$

Examples of the resulting planform functions are provided by rolls, squares, hexagons, regular triangles and the patchwork quilt (Julien & Knobloch 1998). For these solutions $J(h, \nabla_\perp^2 h) \equiv 0$ and all nonlinearities vanish identically, with the exception of the convective flux term in (2.27d) responsible for the distortion of the mean temperature profile. For a given $\widetilde{Ra}$, the reduced equations then collapse into a nonlinear two-point boundary-value problem for the vertical mode structure (Bassom & Zhang 1994; Julien & Knobloch 1999):

$$\partial_Z^2 \Phi + \left(\frac{\widetilde{Ra}\, Nu}{1 + Pr^2\widetilde{k}^2\Phi^2} - \widetilde{k}^6 \right) \Phi = 0, \qquad \Phi(0) = \Phi(1) = 0, \qquad (2.36)$$

valid for all steady planforms h. Here, Nu denotes the non-dimensional heat transport, or Nusselt number ($Nu = -\partial_Z\overline{\theta}\vert_{Z=1} = -\partial_Z\overline{\theta}\vert_{Z=0}$, owing to symmetry), and is determined as an eigenvalue. Since the dependence on Pr can be removed by a simple rescaling of Φ, the resulting $Nu(\widetilde{Ra})$ relation is independent of Pr. Values of Nu for various $\widetilde{Ra}$ are given in table 1.

A comparison of these exact (but non-turbulent) results with the simulation results that follow is informative. For this purpose we give in table 1 the corresponding

numerical values for the mean temperature gradient

$$\partial_Z \bar{\theta} = -\frac{Nu}{1 + Pr^2 \widetilde{k}^2 \Phi^2},$$
(2.37)

at $Z = 1/2$ and $Z = 1$, for various values of $\widetilde{Ra}$. Inspection of equation (2.36) suggests that, for large amplitudes, $\Phi^2 \sim O(\widetilde{Ra}Nu)$, from which it follows that $-\partial_Z \bar{\theta}\big|_{Z=1/2} \propto \widetilde{Ra}^{-1}$. Thus, an isothermal interior develops as $\widetilde{Ra} \to \infty$.

3. Numerical method for simulation of the reduced equations

We examine numerical solutions to the reduced systems (2.27) and (2.29) in a box with dimensions $L_x \times L_y \times 1$ with periodic boundary conditions in the horizontal; periodic boundary conditions are used to approximate a horizontal domain of infinite extent. Note that the physical dimensions of the box are $L_x E^{1/3} H \times L_y E^{1/3} H \times H$. Spatial discretization of (2.27) (for finite Pr number) and (2.29) (for $Pr \to \infty$) is achieved with $N_x/2 \times N_y/2$ Galerkin–Fourier periodic modes in the horizontal. We use a Chebyshev-tau discretization in the vertical (Gottlieb & Orszag 1977) with N_Z modes. The use of Chebyshev modes in the vertical allows a clustering of degrees of freedom near the boundaries, which is desirable for resolving the sharp gradients in $\bar{\theta}$ and θ' that are expected near the upper and lower boundaries. Tau correction is used to enforce boundary conditions (2.30a, b) and (2.31a). In our simulations, spatial and temporal discretization is chosen to resolve all scales; no subgrid-scale modelling is employed.

The systems (2.27) and (2.29) are composed of five independent variables (x, y, Z, t, T). However, following the preliminary investigations of Julien *et al.* (1998), we set $\partial_T \bar{\theta} \equiv 0$ and replace the spatio-temporal averaging over x, y, t by a simple spatial averaging, a procedure supported by the observation that $\partial_T \bar{\theta} \to 0$ as $t \to \infty$. Moreover, for statistically steady states, Julien *et al.* (1998) find that, in a sufficiently large box, the accumulation of averages in t becomes equivalent to horizontally averaging across rising and falling plumes. Accordingly, for the simulations we replace (2.27d) and (2.29d) by

$$\partial_Z \bar{\theta} = -1 + Pr \overline{(\theta' \nabla_\perp^2 \phi - \langle \theta' \nabla_\perp^2 \phi \rangle_Z)},$$
(3.1)

and

$$\partial_Z \bar{\theta} = -1 + \overline{(\theta' \nabla_\perp^2 \phi - \langle \theta' \nabla_\perp^2 \phi \rangle_Z)},$$
(3.2)

respectively, where, as indicated above, the overbar now denotes horizontal spatial averaging and $\langle \cdot \rangle_\xi$ denotes the average operation over an independent variable ξ over $\xi_1 \leqslant \xi \leqslant \xi_2$:

$$\langle f(\xi) \rangle_\xi = \frac{1}{\xi_2 - \xi_1} \int_{\xi_1}^{\xi_2} f(\xi) \, d\xi.$$
(3.3)

For the above, $Z_1 = 0$ and $Z_2 = 1$. As a consequence of this approximation, our results are only valid in the statistically steady-state regime.

Time integration is achieved with a Runge–Kutta method developed by Spalart, Moser & Rogers (1991). Formally, the method is second-order accurate. However, the coefficient on the third-order term is small, and third-order accuracy is observed. In our use of this method, buoyancy, diffusion, and rotation terms are treated implicitly; advection terms and $\nabla_\perp^2 \phi \partial_Z \bar{\theta}$ are treated explicitly. Although it is common to treat rotation terms explicitly, e.g. Julien *et al.* (1996a), our numerical investigations with

$\widetilde{Ra}$	Pr	Box dimensions $\left(E^{1/3}H \times E^{1/3}H \times H\right)$	Grid resolution $N_x \times N_y \times N_Z$	Δt_{avg}
20	1	$10L_c \times 10L_c \times 1$	$64 \times 64 \times 65$	0.196×10^{-1}
20	7	$20L_c \times 20L_c \times 1$	$128 \times 128 \times 65$	0.144×10^{0}
20	∞	$20L_c \times 20L_c \times 1$	$128 \times 128 \times 65$	0.182×10^{-1}
40	1	$10L_c \times 10L_c \times 1$	$96 \times 96 \times 97$	0.498×10^{-2}
40	7	$20L_c \times 20L_c \times 1$	$192 \times 192 \times 97$	0.164×10^{-1}
40	∞	$20L_c \times 20L_c \times 1$	$192 \times 192 \times 97$	0.145×10^{-2}
80	1	$10L_c \times 10L_c \times 1$	$128 \times 128 \times 129$	0.173×10^{-2}
80	7	$20L_c \times 20L_c \times 1$	$256 \times 256 \times 129$	0.472×10^{-2}
80	∞	$20L_c \times 20L_c \times 1$	$256 \times 256 \times 129$	0.405×10^{-3}
160	1	$10L_c \times 10L_c \times 1$	$256 \times 256 \times 257$	0.407×10^{-3}
160	7	$20L_c \times 20L_c \times 1$	$512 \times 512 \times 257$	0.128×10^{-2}
160	∞	$10L_c \times 10L_c \times 1$	$256 \times 256 \times 257$	0.128×10^{-2}

TABLE 2. Model parameters used in the simulations. Horizontal box dimensions are shown as a function of the critical length $L_c = 4.8154$.

this approach exhibited severe CFL (Courant–Friedrichs-Lewy) restriction in time-step size, owing to fast propagating inertial waves on the domain scale. All fields are de-aliased with the standard 2/3 rule at each time substep. Further details regarding spatial and temporal discretization methods are discussed in Appendix A.

Table 2 gives the numbers of spectral modes used for each of the simulations discussed in this paper. Grid resolution was justified *a posteriori*; steady-state solutions were checked to ensure that at least 5 grid points were in the θ' root-mean-square (RMS) boundary layer in the vertical and 10–12 grid points in the mean temperature boundary layer; energy spectra were checked to ensure sufficient resolution in the horizontal.

The evolution to a statistically steady state was found to be insensitive to initial conditions. All solutions were therefore initialized with either random noise or a specified noise-perturbed single-mode pattern (e.g. rolls, squares or hexagons).

4. Results

In this section, we describe the results obtained via numerical simulation of the reduced equations (2.27) and (2.29), with (2.27d) replaced by (3.1), and (2.29d) replaced by (3.2). As discussed in § 3, these equations describe correctly the statistically steady-state regime, but shorten the transient required to reach this state. For numerical simulation in three dimensions, this property is a distinct advantage.

4.1. *Flow morphology*

Our simulations reveal the presence of three distinct flow regimes as $\widetilde{Ra}$ increases. The transitions between these regimes are reflected in both the flow morphology and in statistical measures, and depend on the Prandtl number.

In this section, we describe the morphology of the flow in each of these regimes. Motivated by visualizations in recent laboratory experiments using water (Boubnov & Golitsyn 1986; Sakai 1997; Vorobieff & Ecke 1998, 2002), we begin with $Pr = 7$. Figure 2 shows isometric-view volume-rendered snapshots of the temperature anomaly field θ' for $\widetilde{Ra} = 20$, 40, 80 and 160 taken in a statistically steady state; the Prandtl-number dependence of these results is indicated in figure 3 for $\widetilde{Ra} = 40$. In both
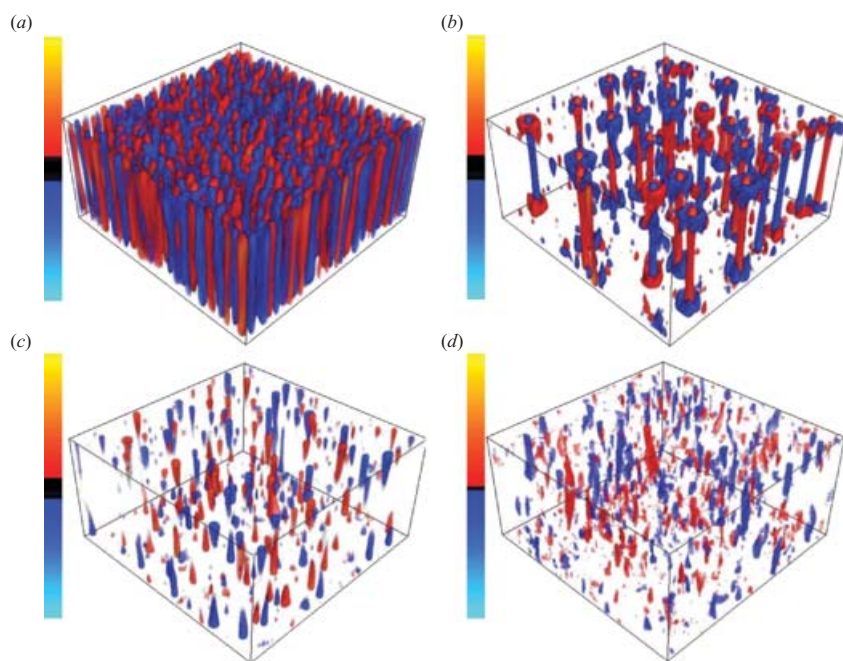
FIGURE 2. Isometric-view snapshots of volume-rendered temperature anomaly θ' for $Pr = 7$ and different Rayleigh numbers $\widetilde{Ra}$. (a) $\widetilde{Ra} = 20$; (b) 40; (c) 80; (d) 160. Colour tables are on the left-hand side of each figure; black regions indicate field values with zero opacity.
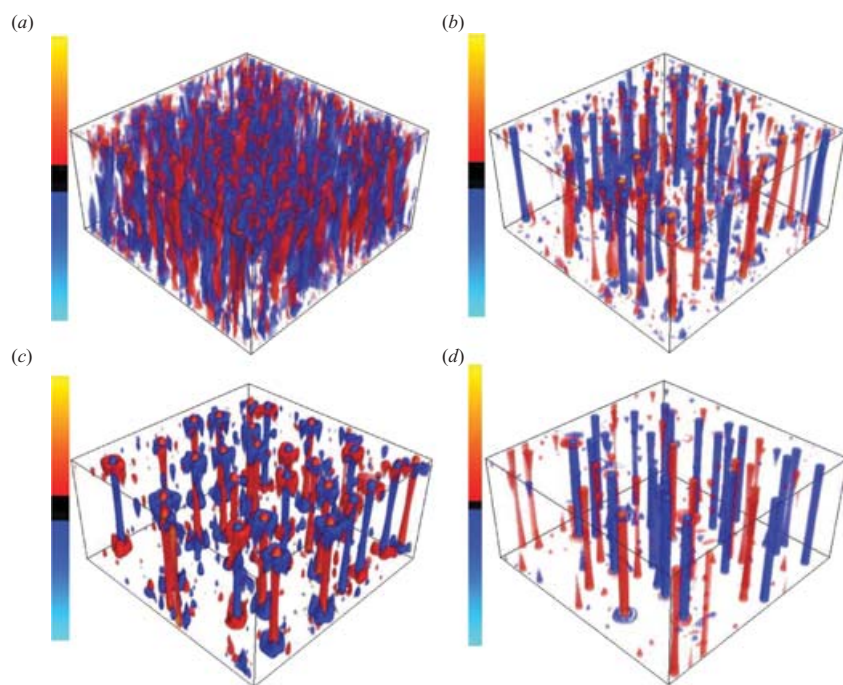

FIGURE 3. As figure 2 but for $\widetilde{Ra} = 40$ and different Prandtl numbers Pr. (a) $Pr = 1$; (b) 3; (c) 7; (d) $\rightarrow \infty$.
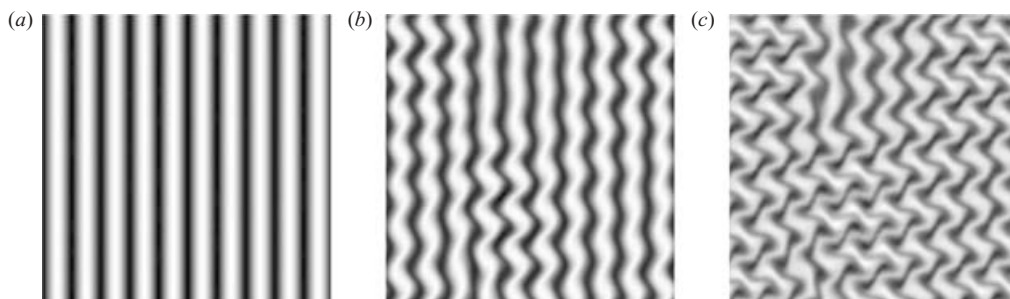
FIGURE 4. Snapshots of vertical vorticity ω'_3 in the (x, y) plane at $Z = 0$ when $\widetilde{Ra} = 20$ and $Pr = 1$, illustrating the development of the zigzag instability. (*a*) $t = 0$; (*b*) $t \approx 7.1$; (*c*) $t \approx 7.7$.

figures, red and blue indicate regions that are, respectively, warm and cold relative to the mean temperature $\overline{\theta}$. The colour tables used in each case are shown on the left-hand side; black regions indicate values for which opacity has been set to zero (i.e. points with temperature in this range are invisible). Guided by the RMS profiles (§ 4.6), opacity distributions were chosen to highlight coherent structures within the flow. The non-dimensional box dimensions are approximately $96 \times 96 \times 1$; the aspect ratio visible in the figure is therefore not to scale. Evidently, for the volumes shown, the computational boxes (in conjunction with periodic boundary conditions) are sufficiently large to represent an infinite fluid layer.

Above the onset value $\widetilde{Ra}_c^{(s)}$, we observe neither the stable cellular states identified by single-mode theory, nor the weakly nonlinear Küppers–Lortz roll-switching states. Instead, perturbed single-mode solutions or random initial states exhibit a short wavelength zigzag type of instability, an example of which is shown in figure 4, which leads to the destruction of the original roll pattern and its replacement for a brief instant by an orthogonal pattern, which then breaks up into a three-dimensional time-dependent state (cf. Cox & Matthews 2000). This state develops into a statistically steady state consisting of a large population of columnar structures spanning the entire depth of the layer. As a consequence, these columns act as very efficient conduits for heat transport, and so carry a large fraction of the heat flux, a property enhanced by their close spacing. This spacing corresponds to the linear stability theory prediction (2.34). Given the primary geostrophic balance inherent in the asymptotic theory, we refer to these structures as thermal Taylor columns. Visualizations of the vertical velocity field w' (not shown) indicate that cold (warm) thermal columns are associated with downwelling (upwelling) fluid. The vorticity field also indicates that each column has an antisymmetric signature in cyclonicity about the midplane $Z = 1/2$. For example, a cold column of downwelling fluid is cyclonic in the upper half of the layer, but has anticyclonic vorticity in the lower half. The opposite is true for warm Taylor columns. This is a consequence of angular momentum conservation in the rotationally constrained regime ($Ro_{conv} \ll 1$), which results in intense cyclonic spin-up and anticyclonic spin-down for accelerating and decelerating fluid parcels, respectively (Boubnov & Golitsyn 1986; Julien *et al.* 1996*a*; Sakai 1997; Vorobieff & Ecke 1998, 2002). However, in no case did we find a stationary vortex grid such as those found by Boubnov & Golitsyn (1986) at moderate Rossby numbers. Instead, the columns are observed to be continuously in motion, devoid of annihilation or merger events, much as observed by Sakai (1997) for $Ro_{conv} \approx 0.1$.

For $\widetilde{Ra} = 40$, the Taylor column population has decreased. Figure 2(*b*) shows the emergence of oppositely signed 'sleeves' surrounding each column. A thorough investigation (see §4.2) shows that these sleeves extend across the layer and are also present in the vertical vorticity and vertical velocity fields. Animations show that the columns now migrate very slowly, an effect we attribute to mutual shielding produced by the sleeves. In the following, we refer to this state as the geostrophic vortex regime, and use the presence of the sleeve in the thermal field as a defining characteristic of this regime. Thresholding of the RMS convective flux $w'\theta'$ as a function of depth indicates that, despite their increased spacing, these vortices transport as much as 60% of the heat flux.

The tendency for increased spacing as a function of Ra at fixed E has been observed in recent experiments and incorporated in scaling laws based on vortex census data (Boubnov & Golitsyn 1986; Sakai 1997). These authors find that the mean separation between neighbouring vortices is proportional to $\widetilde{Ra}^{1/9} E^{1/54}$ (in our scaled parameters), the former using a power-law fit to observations, the latter using a theory that relies on the classical 1/3 heat transport law that is not observed here. Although the predicted dependence on E is weak, in our asymptotic regime any prediction must be independent of E. Given the need for a greater parameter space survey to accumulate census data and the subtleties inherent in vortex selection criteria, we do not pursue similar fits in this paper.

For more aggressive forcing ($\widetilde{Ra} = 80$ and $\widetilde{Ra} = 160$) the Taylor columns are destroyed, and we identify the resulting irregular flow with the geostrophic turbulence regime (Boubnov & Golitsyn 1986), and refer to the coherent structures observed in this regime as thermal plumes. These emanate from upper and lower thermal boundary layers, and consist of two populations, cyclonic and anticyclonic near each. This observation is consistent with the discovery by Vorobieff & Ecke (2002) of a distinct topological change, with decreasing Rossby number, from a single population of cyclonic vortices seen at moderate Rossby numbers ($0.2 < Ro_{conv} < 0.75$) in both experiments and simulations (Julien *et al.* 1996a), to a two-population state consisting of cyclonic and anticyclonic vortices at smaller Rossby numbers. The transition reflects a change in the instability mechanism in the thermal boundary layer from one consisting solely of plume ejection to one that permits, on an equal footing, plume ejection and injection.

In the geostrophic turbulence regime, the column sleeves in the thermal field are largely absent, although they continue to be present in the vertical velocity and vorticity fields (see §4.3). This is a consequence of the destruction in this regime of the coherent columnar conduits that were so efficient at transporting heat. As such, the thermal content (or buoyancy flux) of interior fluid parcels is either continually eroded or completely entrained into the ambient fluid. Indeed, animations in this regime reveal intense vortex–vortex interaction and mergers. The resulting saturation of the mean temperature gradient (see §4.5) is described by the balanced relation

$$Pr\overline{\theta'\nabla_\perp^2\phi}\partial_z\overline{\theta} = -\overline{|\nabla_\perp\theta'|^2}, \tag{4.1}$$

obtained from equation (2.27*c*). We can also derive the following exact relation from equations (2.27*a, b*) together with (4.1):

$$\widetilde{Ra}\overline{|\nabla_\perp^2\theta'|^2} = -Pr^2[\overline{|\nabla_\perp\nabla_\perp^2\phi|^2} + \overline{(\nabla_\perp^2\psi)^2}]\partial_z\overline{\theta}. \tag{4.2}$$

If the dominant dissipation scale is unchanged, these relations indicate that a reduction in buoyancy flux at fixed $\widetilde{Ra}$ and Pr can only be compensated by an increase in the

mean temperature gradient $\partial_Z\overline{\theta}$. Similarly, if a process induces enhanced mixing in θ', while not commensurately mixing ψ and ϕ, then $\partial_Z\overline{\theta}$ must increase. It is therefore the breakdown of the coherent Taylor columns that initiates the saturation of the mean temperature gradient with increasing $\widetilde{Ra}$ discussed in §4.5. Note that if the characteristic horizontal scale of the thermal structure of the column becomes too large radially, it will stretch across the interface between the vortical core of the column and its shielding sleeve. When this happens, the edges of the thermal field of the column will become sheared and mixed with the ambient fluid. This will introduce an irregular buoyancy force just outside the column, which will lead to the demise (if sufficient buoyancy is present) of the well-defined vortical structure of the shielded column. Hence, it is advantageous for column stability for the thermal structure to remain more compact than the vortical structure. As Pr is increased, the thermal structure becomes relatively more compact. This is because, with $Pr \gg 1$, concentration of the temperature field is more easily maintained than concentration of the velocity and vorticity field. Thus, we expect enhanced column stability at larger Pr, i.e. we expect the transition to geostrophic turbulence to be delayed, as discussed next.

Figure 3 shows isometric-view volume-rendered snapshots of θ' at $\widetilde{Ra} = 40$ and $Pr = 1, 3, 7$, and $Pr \to \infty$. While there appear to be coherent structures spanning the depth of the fluid even when $Pr = 1$, these are not the distinct Taylor columns seen for $Pr \geqslant 3$. In fact, for $Pr = 1$, animations demonstrate the presence of strong vortex–vortex interactions and mergers. Furthermore, the saturation in the mean temperature profile for $\widetilde{Ra} \geqslant 20$ (see §4.5) indicates that the geostrophic turbulence regime has been entered, a conclusion supported by the disappearance of temperature sleeves surrounding the plumes. In contrast, the sleeves remain visible for $Pr \geqslant 3$ and the flows remain in the geostrophic vortex regime until $\widetilde{Ra} \approx 40$ ($Pr = 7$), and $\widetilde{Ra} \approx 80$ ($Pr \to \infty$). The convective ring mode seen in some experiments with a free-surface fluid layer driven by a constant heat flux from below (Koschmieder 1967; Boubnov & Golitsyn 1986) cannot be realized in our system with periodic boundary conditions in the horizontal.

4.2. *Structure of Taylor columns*

Owing to subtleties in the trade-off between opacity thresholding and optimization of flow visualization, the structure of the Taylor columns is not completely captured in the volume-rendered snapshots of figures 2 and 3. It is therefore instructive to analyse the horizontal cross-sections of the Eulerian fields.

Figure 5 shows grey-scale cross-sections of the vertical vorticity field ω_3' at the lower boundary ($Z = 0$) for all combinations of $\widetilde{Ra}$ and Pr summarized in table 3. As indicated by the RMS profiles discussed in §4.6, this location corresponds to maximal vertical vorticity. The near-boundary structure of w' and θ' is virtually identical (not shown). Moreover, in the range of $\widetilde{Ra}$ with coherent Taylor columns, $\widetilde{Ra} \lesssim 40$ for $Pr = 7$ and $\widetilde{Ra} \lesssim 80$ for $Pr \to \infty$, cross-sections in all fields taken at different heights demonstrate an extraordinary degree of coherence of these structures in the vertical, and indicate that the Taylor columns are vertically upright and symmetric about the midplane in θ' and w', and antisymmetric in ω_3'. These plots reveal the presence of two populations of shielded vortices consisting of a cyclonic (or anticyclonic) core surrounded by an anticyclonic (or cyclonic) sleeve in the top half of the layer and the reverse in the bottom half. The nature of the fluid flow associated with these Taylor columns can be inferred from the azimuthally averaged line profiles shown in figure 6 for $Pr = 7$ and $\widetilde{Ra} = 40, 80$ and 160. Figure 6 indicates that the profiles of all fields
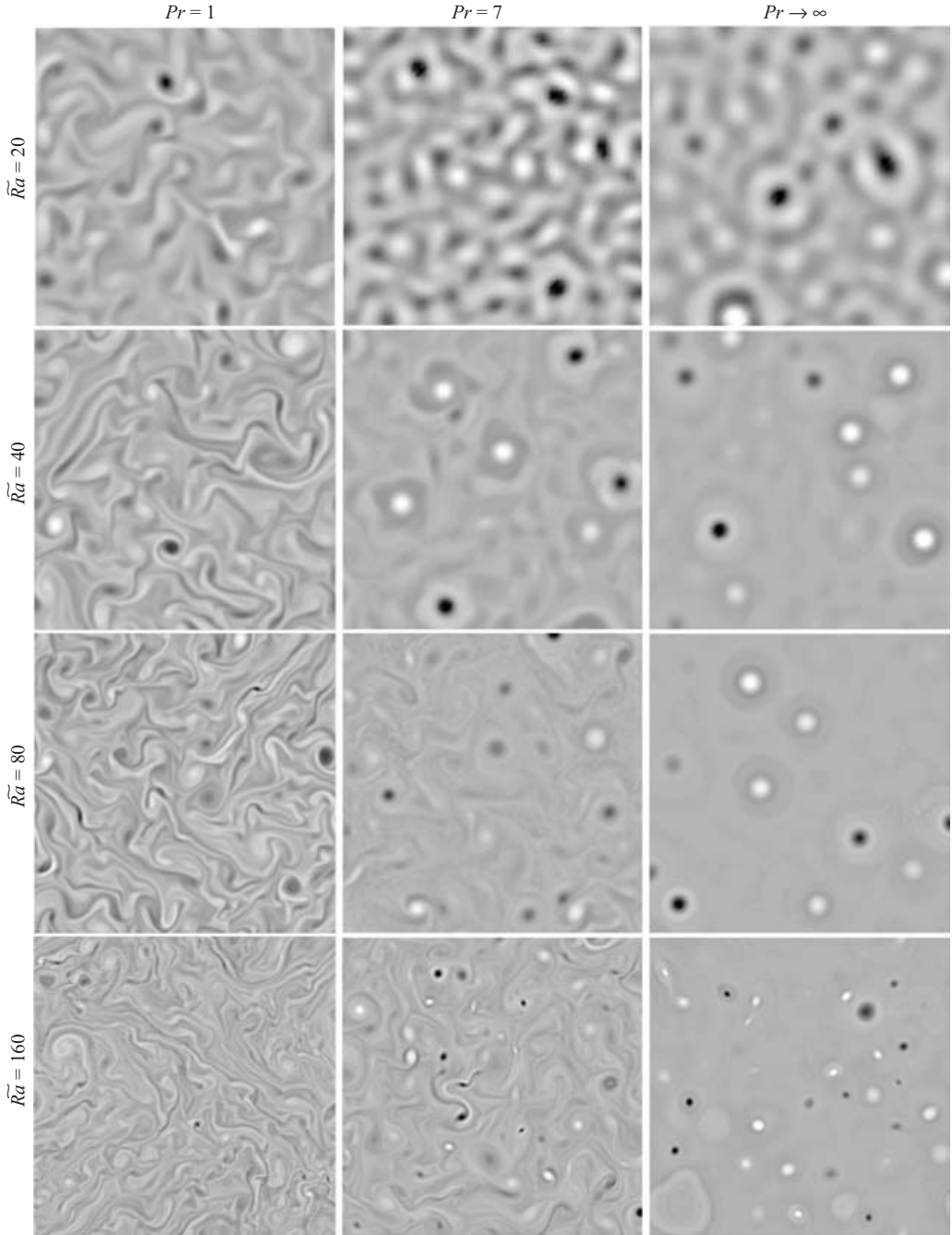
FIGURE 5. Snapshots of vertical vorticity ω_3' in the (x,y)-plane at $Z = 0$ in a statistically steady state. Each snapshot is of a $10L_c \times 10L_c$ section.

are oscillatory and damped. Moreover, the characteristic sizes of the vortex cores in the vertical vorticity and temperature anomaly are virtually identical and always greater than in the profile associated with the vertical velocity. Figure 7 shows fits to the (azimuthally averaged) profiles of temperature, vertical velocity and vertical

$\widetilde{Ra}$	Pr	t_1, t_2	$\langle Nu \rangle_t \pm [\langle (Nu - \langle Nu \rangle_t)^2 \rangle_t]^{1/2}$	$\langle -\partial_Z \overline{\theta}|_{Z=1/2} \rangle_t$
20	1	40.2, 449	4.106 ± 0.129	0.4044
20	7	300, 5249	4.090 ± 0.040	0.3574
20	∞	100, 1509	3.426 ± 0.038	0.3832
40	1	50.0, 615	11.84 ± 0.61	0.3289
40	7	200, 1490	15.53 ± 0.08	0.1813
40	∞	50.2, 265	15.54 ± 0.10	0.1958
80	1	10.0, 173	29.85 ± 1.54	0.3757
80	7	50.2, 254	47.44 ± 0.87	0.1909
80	∞	15.0, 55.0	67.74 ± 0.67	0.1086
160	1	10.0, 30.3	84.87 ± 5.48	0.3773
160	7	15.0, 68.0	102.9 ± 1.94	0.2674
160	∞	8.00, 18.4	292.4 ± 9.8	0.1078

TABLE 3. Values of $\langle Nu \rangle_t$ and the time interval $[t_1, t_2]$ over which the averages are calculated. Also shown are time-averaged mean-temperature gradients calculated at the midplane.
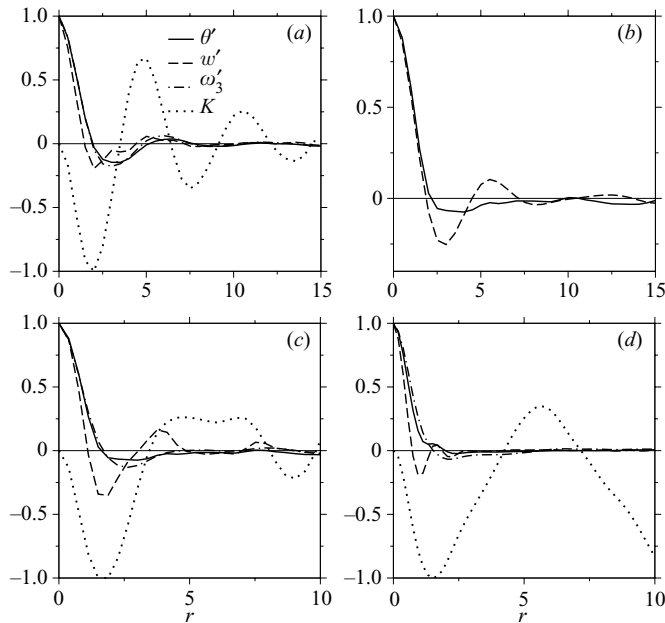
FIGURE 6. Azimuthally averaged radial structure of normalized θ', w', ω'_3, and the circulation K for a typical Taylor column (a, b) and plumes (c, d) when $Pr = 7$. The azimuthal velocity field is defined as $u_\vartheta = K/r$ (not shown). Normalizing values are (69.4, 2.28, 34.5, 22.0) in (a), (14.0, 9.79) in (b), (99.4, 6.79, 95.2, 43.6) in (c), and (316, 31.8, 277, 86.9) in (d). Circulation and vorticity have been omitted in (b) as they are virtually zero at the midplane. (a) $\widetilde{Ra} = 40$, $Z = 0^+$; (b) 40, $\frac{1}{2}$; (c) 80, 0^+; (d) 160, 0^+.

vorticity using trial functions of the form $\alpha \exp(-\beta r) J_0(\zeta r)$, where J_0 is the Bessel function of the first kind and order zero. The fits have a high confidence level and suggest acceptable models for the radial structure of the observed shielded vortices. However, we have not succeeded in deriving exact solutions of this type.
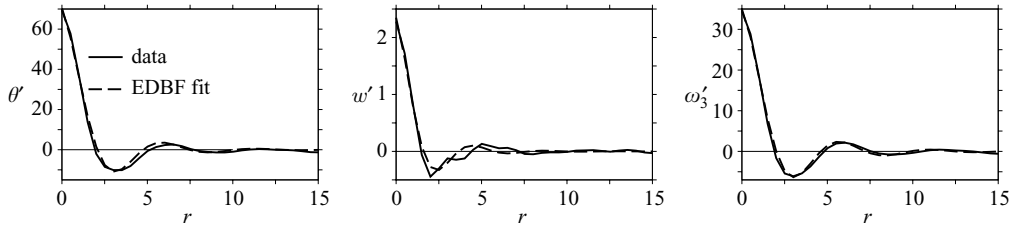
FIGURE 7. Azimuthally averaged radial structure of θ', w', ω_3' at $Z = 0^+$ for a typical Taylor column and $Pr = 7$, $Ra = 40$. Also shown is the fit obtained with an exponentially damped Bessel function (EDBF) of the first kind and zeroth order.
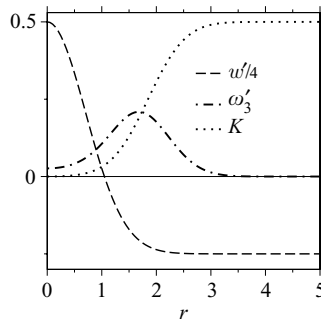

FIGURE 8. Boundary-layer structure of w', ω_3' and circulation K in the Sullivan vortex (Sullivan 1959; Goncharov & Gryanik 1987).

The observed profiles share similarities with those of the Sullivan vortex shown in figure 8 (Sullivan 1959; Goncharov & Gryanik 1987), which constitutes an exact boundary-layer solution to the non-rotating Navier–Stokes equations. However, the Sullivan vortex solution contains only one axisymmetric cell together with a second and much broader cell that extends to infinity. The major differences between the Sullivan solution and the vortices observed in our simulations occur in the vorticity and azimuthal velocity fields (figure 6a). We always find that the maximal vorticity occurs on the column axis and not at some finite distance away from it. Moreover, the sleeves associated with our vortices are characterized by reversals in both vorticity and azimuthal velocity, a property not shared by the Sullivan vortex. Significantly, figure 6(a) shows that, as a consequence of the vortex core–sleeve structure, the circulation decays to zero at infinity. The resulting shielding implies that the vortices interact only weakly, behaving like dilute particles with zero circulation. In contrast, Sullivan vortices (figure 8) have finite circulation at infinity, and therefore interact strongly.

To our knowledge, there is no definitive experimental study of convective vortex structures in the geostrophically controlled limit, although Vorobieff & Ecke (1998, 2002) are able to deduce velocity fields and instantaneous streamlines using PIV measurement techniques. However, no data on the spatial structure of the vorticity field is available, and the detection of a weak counter-cell appears to be at the resolution limit of this technique.

4.3. *Thermal plumes*

Our numerical simulations indicate that the Taylor columns lose stability for large enough $\widetilde{Ra}$ ($\widetilde{Ra} > 10$ for $Pr = 1$; $\widetilde{Ra} > 40$ for $Pr = 7$; $\widetilde{Ra} > 80$ for $Pr \rightarrow \infty$), and are replaced by thermal plumes. These are typically non-axisymmetric, although

evidence for a shielding sleeve structure in the vorticity and velocity fields after the transition can be identified (figure 6*c*, *d*). However, the plumes now have strong finite net circulation (figure 6*b*, *c*), and are thus exposed to strong interaction forces expected of unshielded vortices (figure 5). We surmise therefore that the Taylor columns lose stability through a deshielding process that results in the development of a net circulation that exposes the column to strong long-range interaction forces, and conjecture that this is the process that leads to the transition between what experimentalists refer to as the 'vortex-grid' regime and the regime of irregular geostrophic turbulence.

If we adopt the view that plumes are merely ejected pieces of an unstable thermal boundary layer, it follows that in the geostrophic turbulence regime the horizontal scale of the plumes will decrease with increasing $\widetilde{Ra}$ as a consequence of the decreasing thickness of the thermal boundary layer. The mean spacing between plumes also decreases as $\widetilde{Ra}$ increases. This leads to an increased plume number density and significant plume–plume interaction. The resulting vortex dynamics are, in fact, reminiscent of interactions between shielded vortices (Carton 1992). Specifically, in addition to mergers of like-signed vorticity, we also observe peripheral interactions leading to streamer formation without interactions between the cores. This is reflected in the preponderance of filamentary streaks in the $Pr = 1$ solutions (see figure 5). The long filamentary streaks of opposite vorticity are signatures of such pairings. Similar behaviour is seen in the barotropic instability of isolated shielded vortices (Carton 1992). Finally, plumes with tripole structure can also be identified (see, e.g. the results for $\widetilde{Ra} = 80$ and $Pr = 7$ in figure 5).

4.4. *Heat transport*

The statistical quantity of primary interest is the mean heat flux across the fluid layer. In the statistically stationary regime, this flux is independent of height, and can therefore be measured at one of the boundaries. In our simulations, we track the Nusselt number at the top of the layer, namely, $Nu = -\partial_Z \overline{\theta}|_{Z=1}$. The mean temperature gradient is in turn given by equations (3.1) and (3.2) according to whether Pr is finite or infinite. In the absence of convection, $\overline{\theta} = 1 - Z$ and $Nu = 1$. The dependence of Nu on the non-dimensional parameters Ra and E has been of particular interest to both theorists and experimentalists ever since Rossby's original survey (Rossby 1969). In fact Nu depends on Pr as well as the domain aspect ratio A and the boundary conditions. In the limit of rapid rotation, $E^{1/3} \ll 1$, appropriate for our reduced equations, predictions valid for $Pr \gg \infty$ include

$$Nu = \frac{1}{256} x^3 \left(1 + \frac{3}{x}\right)^4, \qquad x \equiv \frac{\widetilde{Ra}}{\widetilde{Ra}_c^{(s)}}, \tag{4.3}$$

based on a parameter-free turbulence model (Canuto & Dubovikov 1998), and

$$Nu = C \, \widetilde{Ra}^3, \tag{4.4}$$

where C is a constant, obtained by variational methods (Chan 1974; Hunter & Riahi 1975; Riahi 1977). These predictions should be compared with the upper-bound result for $Pr \gg 1$ (Constantin, Hallstrom & Putkaradze 1999, 2001)

$$Nu \leqslant 1 + C \, Ra^{2/5} \equiv 1 + C \, E^{-8/15} \widetilde{Ra}^{2/5}. \tag{4.5}$$

In contrast, numerical simulations by Julien *et al.* (1996*b*) and subsequent laboratory experiments by Liu & Ecke (1997) clearly demonstrate that, at fixed convective Rossby
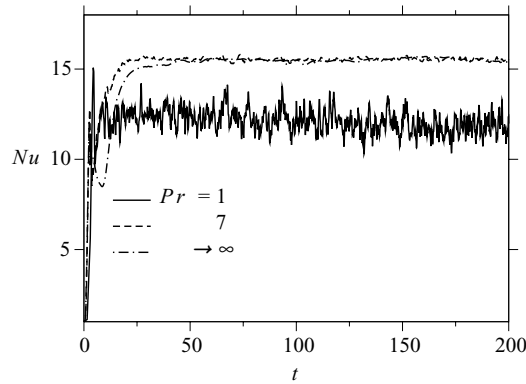
FIGURE 9. Representative Nu histories for $\widetilde{Ra} = 40$ and $Pr = 1$, 7, and $Pr \rightarrow \infty$. Time is in units of the horizontal thermal diffusion time.

number $Ro_{conv} = E^{1/3}\sqrt{\widetilde{Ra}/Pr}$, the Nusselt number scales like

$$Nu = a_0 + a_1 \widetilde{Ra}^{a_2}, \qquad (4.6)$$

where a_0, a_1 and a_2 denote coefficients that depend on Ro_{conv}, Pr, A and the boundary conditions. This relation is equivalent to the relation $Nu = a_0 + a_1(Ra^{a_2} - Ra_c^{a_2})$ used by Julien *et al.* (1996*b*); the more commonly used power-law fit $Nu = a_1 Ra^{a_2}$ follows from the assumptions that $Nu \gg 1$, $Ra \gg Ra_c$. In particular, in the regime $10^5 \leqslant Ra \leqslant 5 \times 10^8$, $1.41 \times 10^{-5} < E \leqslant \infty$ and $1 \leqslant Pr \leqslant 7$, covering $0.1 \leqslant Ro_{conv} < \infty$, the simulations reveal that the classical exponent $a_2 = 1/3$ (Priestley 1959) arises for free-slip boundaries only, while for rigid boundaries one finds instead the hard turbulence exponent $a_2 = 2/7$ (Siggia 1994). The reduced Rayleigh number covered by these investigations spans $\widetilde{Ra}_c^{(s)} \leqslant \widetilde{Ra} \leqslant 135$. Unfortunately, we know of no predictions of the dependence of Nu on Ro_{conv} and so cannot connect these results to those valid in the regime of interest, namely, $E \ll 1$.

Figure 9 shows representative results obtained for $\widetilde{Ra} = 40$ and three values of the Prandtl number, $Pr = 1$, 7 and $Pr \rightarrow \infty$, as a function of the horizontal thermal diffusion time. This time scale requires that we replace t by $Pr\,t$, and is used to facilitate comparison of the finite Pr results with those obtained for $Pr \rightarrow \infty$. The usefulness of the reduced equations is immediately apparent; in all cases, the solutions relax rapidly to a statistically steady state after a brief adjustment period. This occurs irrespective of whether the initial condition is a single-mode solution (not shown) or a perturbed conductive state (shown), the latter providing the gravest constraint. For this value of $\widetilde{Ra}$, the Nusselt number traces for $Pr = 7$ and $Pr \rightarrow \infty$ are nearly identical, and the average is substantially higher than that for $Pr = 1$. This is expected because the vertical transport is more efficient at higher Pr where the flow is organized into efficient heat transport columns, while the $Pr = 1$ vortices are sleeveless and heat transport is reduced owing to lateral mixing. For other values of $\widetilde{Ra}$, the Nusselt numbers at $Pr = 7$ and $Pr \rightarrow \infty$ are not so similar (see table 3). Note that the non-dimensional time for one rotational period is $4\pi E^{1/3}/Pr$ (see § 2.4). Thus, the results shown in figure 9 span very many rotation times. In addition, the $Pr = 1$ solution exhibits prominent fluctuations about the mean. This is to be expected. First and foremost, momentum fluctuations in the $Pr = 7$ and $Pr \rightarrow \infty$ systems are suppressed rapidly owing to increased viscous diffusion, yielding a relatively smooth
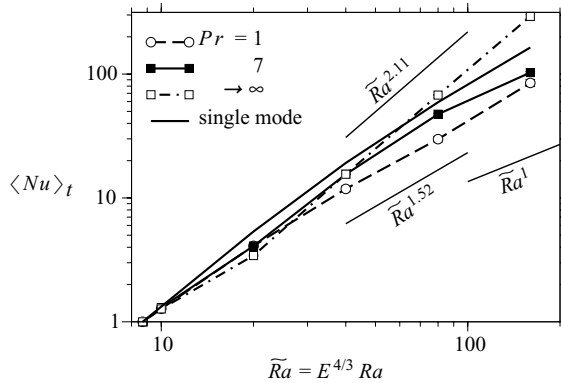
FIGURE 10. Time-averaged heat transport $\langle Nu \rangle_t$ as a function of the scaled Rayleigh number $\widetilde{Ra}$. Also shown are the best-fit power laws $\widetilde{Ra}^{2.11}$, $\widetilde{Ra}^{1.52}$ and $\widetilde{Ra}^{1}$.

time-dependent heat flux ($\overline{w'\theta'}$). Secondly, the computational box size employed in the $Pr = 7$ and $Pr \to \infty$ cases is twice that for $Pr = 1$, and fluctuations in these cases are therefore reduced when computing horizontal averages.

Table 3 shows the time-averaged Nusselt number $\langle Nu \rangle_t$, together with the averaging interval $t_1 < t < t_2$ within which the system was deemed to be statistically stationary, and the mean temperature gradient at mid-layer, $-\partial_Z\overline{\theta}\big|_{Z=1/2}$. Also listed are the RMS values of $Nu - \langle Nu \rangle_t$, i.e. $[\langle (Nu - \langle Nu \rangle_t)^2 \rangle_t]^{1/2}$. Figure 10 summarizes the behaviour of $\langle Nu \rangle_t$ as a function of the scaled Rayleigh number $\widetilde{Ra}$ for various Pr values. The symbols in the figure are larger than the error bars corresponding to the RMS values in table 3. For comparison, the figure also shows the values of $\langle Nu \rangle_t$ obtained from the single-mode theory of Bassom & Zhang (1994) and Julien & Knobloch (1998, 1999) discussed in §2.8. We see that the single-mode solutions consistently provide an upper bound for the heat transport when $Pr = 1, 7$. This is not so, however, as $Pr \to \infty$. In this regime, we find that the fluid self-organizes into a highly efficient state of heat transport that surpasses the single-mode result once $\widetilde{Ra} \geqslant 80$. Referring to §4.1, we see that this property of the flow is a consequence of the presence of extremely stable columnar structures.

We use the data summarized in table 3 to obtain fits to the relation $Nu = Nu(\widetilde{Ra}, Pr)$. For this purpose we consider power-law fits of the form

$$\langle Nu \rangle_t = a_0 + a_1 \widetilde{Ra}^{a_2}, \qquad \langle Nu \rangle_t = b_0 + b_1(\widetilde{Ra} - \widetilde{Ra}_c^{(s)})^{b_2}. \qquad (4.7)$$

The constants obtained from fits to the data for $20 \leqslant \widetilde{Ra} \leqslant 160$ are given in table 4. The fits indicate that the exponents are bracketed by the intervals $1.2 \lesssim a_2 \lesssim 2.1$ and $1 \lesssim b_2 \lesssim 2$. The single-mode theory indicates that, for the values of $\widetilde{Ra}$ used, the Nusselt number is not in the asymptotic regime characterized by the scaling $Nu \sim Ra \log(RaNu)$ (Julien & Knobloch 1999). The fitted exponents also show that the scaling exponent in (4.4) is too large for $Pr \to \infty$, and therefore represents an upper bound. However, we find no correlation between the $Pr \to \infty$ results obtained here and the prediction (4.3) put forward by Canuto & Dubovikov (1998); this prediction dramatically underestimates the heat transport. Our results are, however, consistent with the upper bound found by Constantin et al. (2001), although they indicate that this bound overestimates transport by a large factor, namely, $O(E^{-8/15})$.

	a_0	a_1	a_2	NRMS error	b_0	b_1	b_2	NRMS error
$Pr = 1$	0.965	0.037	1.521	9.6×10^{-3}	2.670	0.057	1.450	1.1×10^{-2}
$Pr = 7$	0.000	0.175	1.258	5.3×10^{-2}	-5.051	0.733	0.995	2.3×10^{-2}
$Pr \to \infty$	0.000	0.007	2.112	8.1×10^{-4}	-2.030	0.015	1.971	2.1×10^{-3}

TABLE 4. Fitted values of the parameters in the functions $\langle Nu \rangle_t = a_0 + a_1 \widetilde{Ra}^{a_2}$ and $\langle Nu \rangle_t = b_0 + b_1 (\widetilde{Ra} - \widetilde{Ra}_c^{(s)})^{b_2}$ from the data shown in table 3. Also shown is the normalized RMS (NRMS) error for the fits.
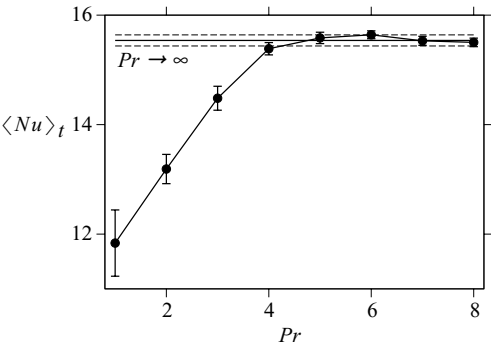
FIGURE 11. Time-averaged heat transport $\langle Nu \rangle_t$ as a function of Pr for $\widetilde{Ra} = 40$. Dashed lines about the solid line for $Pr \to \infty$ correspond to the RMS error bars.

Figure 10 reveals that, at fixed $\widetilde{Ra} \leqslant 40$, the dependence of $\langle Nu \rangle_t$ on Pr is non-monotonic. When $\widetilde{Ra} = 40$ $\langle Nu \rangle_t$ increases with Pr to a maximum at $Pr \approx 6$ (see figure 11) before decreasing to the $Pr \to \infty$ value. Similar non-monotonic dependence on Pr has been observed in simulations of non-rotating Rayleigh–Bénard convection (Kerr & Herring 2000). Evidently, certain Prandtl numbers favour spatial structures that enhance heat transport, although detailed understanding of this process remains elusive.

Comparison of the data shown in figure 3 with the $\langle Nu \rangle_t$ *vs. Pr* data in figure 11 illustrates a connection between effectiveness of heat transport and flow structure. In particular, for $\widetilde{Ra} = 40$, we found that $\langle Nu \rangle_t$ was maximum when $Pr = 6$, while figure 3 shows that the case $Pr = 7$ has the most distinct columnar and sleeve structure (of those shown).

4.5. *Mean temperature distribution*

As a measure of efficiency of vertical mixing, it is instructive to examine the profiles of the mean temperature $\bar{\theta}$ and their midplane gradients $-\partial_Z \bar{\theta}|_{Z=1/2}$ as a function of $\widetilde{Ra}$; these quantities are shown in figures 12 and 13, respectively. The corresponding single-mode results are included for comparison. The latter evolve towards an isothermal interior with increasing $\widetilde{Ra}$; in particular, the midplane mean temperature gradient obtained from these solutions decreases like $\widetilde{Ra}^{-1}$, as discussed in §2.8. Similar behaviour is observed in non-rotating turbulent Rayleigh–Bénard convection, but not in the reduced equations. Figure 13 shows that, for all Pr, the mean temperature gradient initially decreases monotonically, much as expected from the single-mode
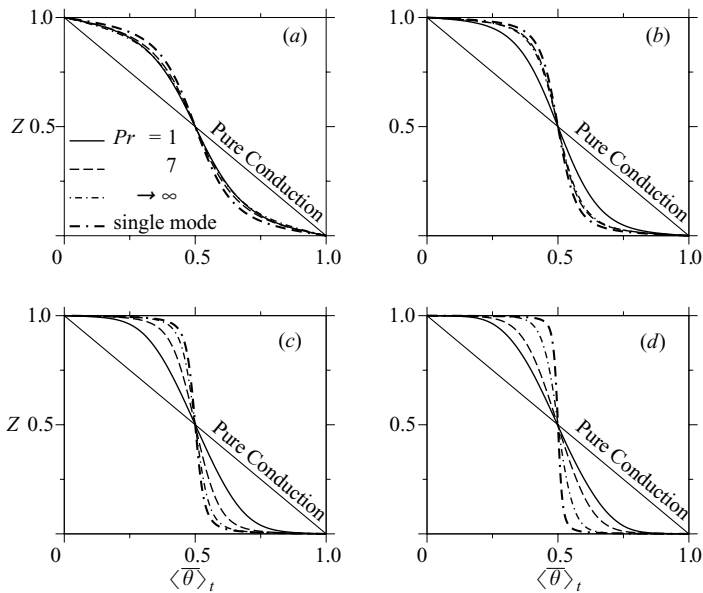
FIGURE 12. Time-averaged mean temperature profiles for different values of Pr. The single-mode solution is shown for comparison. (*a*) $\widetilde{Ra} = 20$; (*b*) 40; (*c*) 80; (*d*) 160.
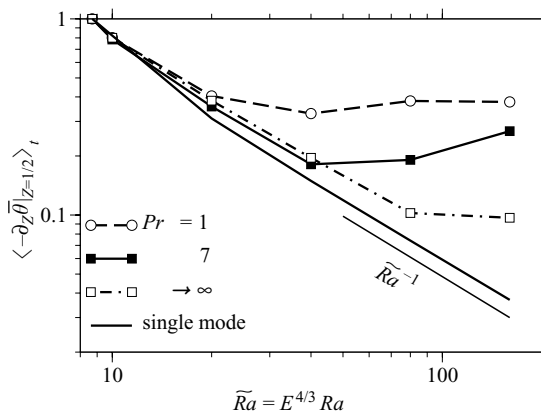

FIGURE 13. Time-averaged mean temperature gradient $-\partial_Z \bar{\theta}$ at the midplane of the fluid layer ($Z = 1/2$) for different Pr as a function of $\widetilde{Ra}$. The single-mode solution is shown for comparison.

results, but then saturates at some finite $\widetilde{Ra}$. For $Pr = 1$, this occurs for $\widetilde{Ra} \geqslant 20$, while for $Pr = 7$ and $Pr \to \infty$ the saturation appears to take place at $\widetilde{Ra} \approx 40$ and $\widetilde{Ra} \approx 80$, respectively. However, for these Prandtl numbers, the saturation process becomes so slow that without expensive computation we cannot establish that saturation has in fact occurred in $\widetilde{Ra} \lesssim 160$. However, it is clear that even if complete saturation has not been reached, the behaviour of the system departs dramatically at these parameter values from the single-mode results and indeed from the behaviour familiar from non-rotating Rayleigh–Bénard convection.

	a_0	a_1	a_2	NRMS error	b_0	b_1	b_2	NRMS error
$Pr = 1$	0.001	38.08	-2.102	1.2×10^{-2}	-0.001	2.014	-1.376	4.1×10^{-3}
$Pr = 7$	0.000	36.60	-2.085	6.3×10^{-3}	-0.001	2.003	-1.369	1.3×10^{-2}
$Pr \to \infty$	0.000	84.02	-2.305	3.5×10^{-3}	-0.001	3.421	-1.521	3.3×10^{-3}

TABLE 5. Fitted values of the parameters in the functions $\Delta_{BL} = a_0 + a_1 \widetilde{Ra}^{a_2}$ and $\Delta_{BL} = b_0 + b_1(\widetilde{Ra} - \widetilde{Ra}_c^{(s)})^{b_2}$ for $20 \leqslant \widetilde{Ra} \leqslant 160$. Also shown is the normalized RMS (NRMS) error for the fits in the above range.

As discussed in §4.1, we attribute this unexpected behaviour to enhanced lateral mixing owing to the inherently vortical nature of the flow, as suggested by the exact relations (4.1)–(4.2). The former states that buoyancy production by extraction of heat from the mean temperature profile is balanced by thermal dissipation in the horizontal. Our simulations indicate that prior to saturation $\nabla_\perp^2 \phi \, \theta' \sim O(\widetilde{Ra}^\gamma)$, $\gamma > 0$, while $\partial_Z \overline{\theta} \sim O(\widetilde{Ra}^{-\alpha})$, $\gamma > \alpha > 0$. Thus, horizontal dissipation scales like $\widetilde{Ra}^{\gamma - \alpha}$, in contrast to the single-mode result $\log(\widetilde{Ra}Nu)$. However, once the profile saturates, horizontal dissipation becomes $O(\widetilde{Ra}^\gamma)$ and therefore increases more rapidly with $\widetilde{Ra}$ than in the initial phase. The appearance of these two regimes correlates well with the absence or presence of coherent structures that span the depth of the fluid layer, as discussed in §4.1.

4.6. *Flow statistics*

In this section, we examine the vertical profiles of the time averages of the root-mean-square temperature anomaly $[\theta']_{RMS}$, vertical velocity $[w']_{RMS}$, and vertical vorticity $[\omega'_3]_{RMS}$, where, for any function f, $[f]_{RMS} := \langle ((\langle \langle f^2 \rangle_x \rangle_y)^{1/2} \rangle_t$. Figure 14 shows the profiles of these fields in $1/2 \leqslant Z \leqslant 1$ for the cases shown in figure 10; the profiles in $0 \leqslant Z \leqslant 1/2$ are obtained by reflection in $Z = 1/2$. For the purpose of comparison with the $Pr \to \infty$ results, we have scaled the vertical velocity and vertical vorticity results for $Pr = 7$ using the scaling $Pr \, w' \to w'$ and $Pr \, \omega'_3 \to \omega'_3$.

We see that the $[\theta']_{RMS}$ boundary-layer thickness Δ_{BL} decreases rapidly with increasing $\widetilde{Ra}$, indicating the formation of a thermal boundary layer. In our computations, the Chebyshev-grid distribution was such that Δ_{BL} was resolved with at least five nodes in all cases. As with our quantification of the scaling of $\langle Nu \rangle_t$, we fit the boundary-layer thickness data to the relations

$$\Delta_{BL} = a_0 + a_1 \widetilde{Ra}^{a_2}, \qquad \Delta_{BL} = b_0 + b_1(\widetilde{Ra} - \widetilde{Ra}_c^{(s)})^{b_2}. \qquad (4.8)$$

Table 5 lists the values of the constants obtained from fits to the data for $20 \leqslant \widetilde{Ra} \leqslant 160$. For $Pr = 1$ and 7 we find that $a_2 \approx -2$ and $b_2 \approx -1.4$, while for $Pr \to \infty$, $a_2 \approx -2.3$ and $b_2 \approx -1.5$. We have insufficient data to make a judgement on the scaling with respect to Pr.

All three fields exhibit a general trend. At lower $\widetilde{Ra}$, the profiles for $Pr = 7$ and $Pr \to \infty$ are similar; the similarity is strongest at $\widetilde{Ra} = 40$. However, for more aggressive forcing this resemblance ceases, and the $Pr = 7$ profiles begin to resemble those for $Pr = 1$. From the results in §4.1, we find that these trends are directly linked to the flow structure within the layer.

The vertical vorticity profiles for $\widetilde{Ra} = 20$, 40 and $Pr = 7$, $Pr \to \infty$ are indicative of flow dominated by columnar structures spanning the fluid layer, as illustrated in

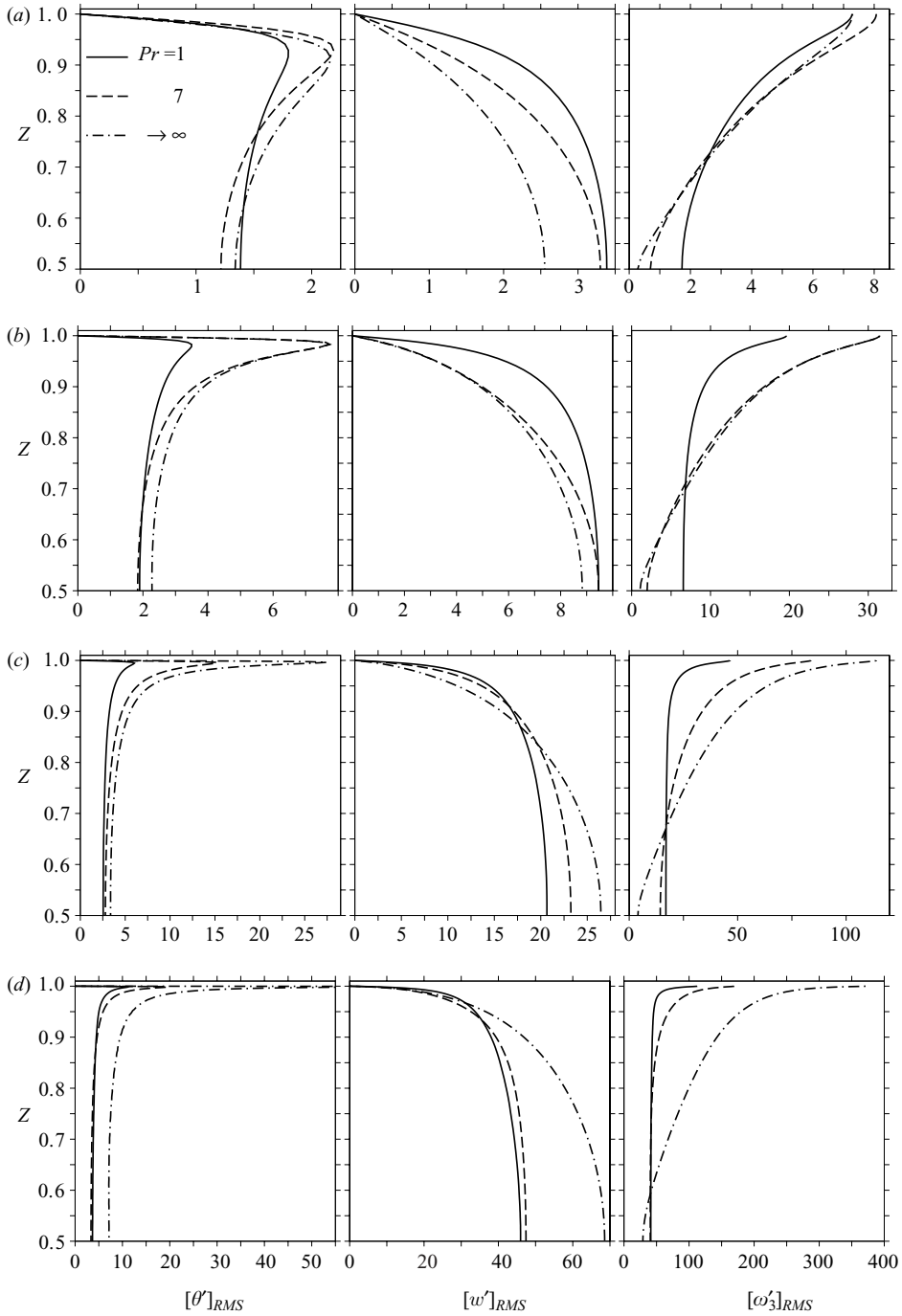FIGURE 14. Vertical profiles of the RMS temperature anomaly θ' (left-hand panels), the RMS vertical velocity w' (middle panels), and the RMS vertical vorticity ω_3' (right-hand panels), showing the development of a thermal boundary layer with increasing $\widetilde{Ra}$. Only the top half of the domain is shown; the profiles in the lower half are obtained by reflection in $Z = 1/2$. The $Pr = 7$ results have been scaled using $(Pr\ w') \to w'$ and $(Pr\ \omega_3') \to \omega_3'$. (a) $\widetilde{Ra} \equiv E^{4/3} Ra = 20$; (b) 40; (c) 80; (d) 160.
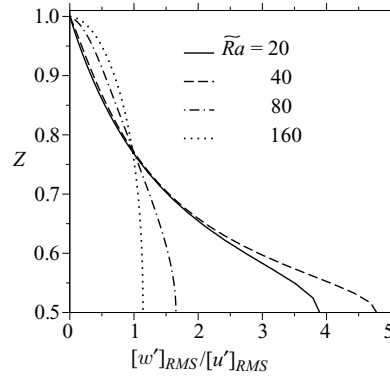
FIGURE 15. Vertical profiles of the ratio of RMS vertical and horizontal velocities ($[w']_{RMS}/[u']_{RMS}$) for $Pr = 7$. Only the top half of the domain is shown; the profiles in the lower half are obtained by reflection in $Z = 1/2$.

figures 2 and 3. Vorticity is injected at the boundaries and monotonically decays to a minimum at the layer centre. The profiles also indicate that the flow approaches a uniform state throughout the interior as $\widetilde{Ra}$ increases. This is most clearly seen in the $Pr = 1$ and $Pr = 7$ profiles. This uniform state in the interior is indicative of a fluid that is well mixed through horizontal advection.

Finally, in figure 15, we show profiles of the ratio $[w']_{RMS}/[u']_{RMS}$ for $Pr = 7$ and $20 \leqslant \widetilde{Ra} \leqslant 160$ in the top half of the layer; corresponding profiles for $[w']_{RMS}/[v']_{RMS}$ are identical. The figure shows that when Taylor columns are present, vertical motions dominate over horizontal ones at mid-layer, while in the geostrophic turbulence regime, the flows are almost isotropic. These results are a reflection not only of the columnar structure of the Taylor vortices in the geostrophic vortex regime, but also of their spatial organization. They are also indicative of the breakdown of the columnar structure in the geostrophic turbulence regime.

5. Conclusions

In this paper, we have examined the low-Rossby-number regime of Rayleigh–Bénard convection. To overcome the limitations imposed by the simultaneous requirement to resolve both fast inertial waves and thin viscous boundary layers at the top and bottom of the layer we derived an asymptotically exact set of reduced equations that captures much of the behaviour of Rayleigh–Bénard convection in this regime. The reduced equations are derived by a systematic expansion procedure that assumes that the dominant structures possess a small horizontal scale and that the Rossby number based on this scale is also small. The resulting equations incorporate Taylor–Proudman balance at leading order and are valid outside of the (passive) boundary layers, i.e. in the bulk. This system of equations is of second order in the vertical, and retains inertial waves on the scale of the depth of the layer only, i.e. fast inertial waves whose vertical scale is comparable to the horizontal scale are filtered out. The resulting system of equations is therefore amenable to extensive direct numerical simulations, and similar computational advantages are likely to exist for large-eddy simulations as well. In view of the extra reflection symmetry present at leading order in the reduced system, preference for cyclonic structures over anticyclonic ones is lost, an observation consistent with recent low Ro experiments.

These structures are all in geostrophic balance despite their small horizontal scale, and hence can be identified with Taylor columns.

Our simulations have revealed the presence of three distinct regimes of turbulent convection. For relatively small values of the scaled Rayleigh number $\widetilde{Ra}$, the Taylor columns extend across the layer depth, with mean separation of the order of the linear theory wavelength. With increasing $\widetilde{Ra}$, this Taylor column regime gives way to more intense but sparser Taylor columns with opposite-sign sleeves that shield nearby columns and extend across the layer. As a result, the columns move more slowly and retain their integrity over long times. Moreover, because of the more intense up- and down-drafts in these columns, this regime is more efficient at vertical heat transport. The resulting state resembles the geostrophic vortex regime seen in experiments, although no 'freezing' into an ordered lattice takes place. With increasing $\widetilde{Ra}$, the integrity of these columnar structures decreases and the columns are replaced by long-lived structures that no longer penetrate the layer. The sleeves disappear and with them the shielding of nearby vortices. As a result, we see sharply increased interactions, and surmise that these are, in turn, responsible for the loss of integrity of the columnar structures. These changes are accompanied by a reduction in the efficiency of heat transport, and homogenization of the RMS velocity. We have identified this regime with the geostrophic turbulence regime seen in experiments.

Our simulations indicate that the delineation of each of these regimes is quite sharp, and that the morphological transitions we see in the flow are also reflected in a variety of statistical measures such as the Nusselt number, mid-layer temperature gradient and RMS velocities. This fact made it relatively easy to follow the transitions as a function of the Prandtl number.

We have also seen that the inherent vortical nature of rapidly rotating flows leads to significant lateral mixing at all Prandtl numbers. In most oceanic general circulation models, convection is an unresolved process that must be parameterized. However, most schemes used for this purpose (Marshall & Schott 1999) account only for mixing in the vertical. Our simulations suggest, however, that lateral mixing should also be incorporated in parameterizations of water mass transfer, and mixing of salinity, density and temperature occurring on scales of several kilometres. Experiments by Levy & Fernando (2002) have clearly illustrated the non-negligible role of lateral mixing at low Ro for a deepening mixed layer.

The shielding of the vortices we see in the geostrophic vortex regime suggests that models based on weakly interacting vortices may well provide a better description of this regime than those based on strongly interacting localized structures such as Sullivan vortices (favoured by Boubnov & Golitsyn 1995; Vorobieff & Ecke 1998, 2002) or 'hetons' (Legg & Marshall 1998; Marshall & Schott 1999). An alternative model incorporating buoyancy forcing has been derived by Kuo (1966).

We do not currently understand why in some experiments the vortices tend to organize themselves into a lattice. Three possible explanations suggest themselves. The first is simply that some experiments are performed at finite Rossby numbers, and this affects the stability of the lattice state. Such a state is admitted by our reduced equations, and can be computed semi-analytically if all the vortices are taken to be identical. The second is that the transition is associated with the breaking of symmetry between cyclonic and anticyclonic vortices; vortex lattices have not been observed in systems with such a symmetry and therefore under low-Rossby-number conditions. Finally, it is possible that weak large-scale circulations driven by lateral walls and centrifugal forces advect the vortices and in effect replace the

vortex–vortex interactions that are lost owing to shielding. In some experiments (Boubnov & Golitsyn 1986), the rotational Froude number Fr_Ω can be as large as 0.34, suggesting that centrifugally driven flows may well be responsible for the observed crystallization of the Taylor columns into triangular grids in the geostrophic vortex regime (Boubnov & Golitsyn 1986). Experiments by Hart, Kittelman & Ohlsen (2002) indicate that the behaviour of such large-scale circulation undergoes significant changes with decreasing Rossby number.

Appendix A. Numerical simulation details

In this Appendix, we discuss details of our numerical method for solving the system (2.27) subject to boundary conditions discussed in §2.6, but in the absence of slow-time variation as discussed in §3.

A.1. *Horizontal spatial discretization*

We discretize with $N_x \times N_y$ evenly spaced nodes in the horizontal directions and use a discrete Fourier transform (DFT) for all dependent variables. To this end, we expand dependent variables $\boldsymbol{w}(x, y, Z, t) := (\theta', \phi, \psi)^T$ as

$$\boldsymbol{w} = \sum_{j=0}^{N_y/2-1} \sum_{i=0}^{N_x/2-1} \left[\widetilde{\boldsymbol{w}}_{ij}^c(Z, t) \cos(k_{x,i}x + k_{y,j}y) + \widetilde{\boldsymbol{w}}_{ij}^s(Z, t) \sin(k_{x,i}x + k_{y,j}y) \right], \quad \text{(A 1)}$$

where $k_{x,i} = i\pi/L_x$, $k_{y,j} = j\pi/L_y$ are the associated discrete wavenumbers, and $\widetilde{\boldsymbol{w}}^c$, $\widetilde{\boldsymbol{w}}^s$ are the Fourier coefficients. We may readily transform quantities from physical space to spectral, space with a DFT, which we denote $\widetilde{\boldsymbol{w}} = \mathscr{F}(\boldsymbol{w})$. Substitution of (A 1) into the governing equations, multiplication by $[\cos(k_{x,m}x + k_{y,n}y) + \sin(k_{x,m}x + k_{y,n}y)]$, and integration over $[0, L_x]$ in x and $[0, L_y]$ in y yields a system of $N_x \times N_y$ equations in spectral space, one for each $\widetilde{\boldsymbol{w}}_{ij}^c$ and $\widetilde{\boldsymbol{w}}_{ij}^s$. These can be written as

$$\boldsymbol{M} \cdot \partial_t \widetilde{\boldsymbol{w}}_{ij} + \boldsymbol{N} = \boldsymbol{L} \cdot \widetilde{\boldsymbol{w}}_{ij}, \quad \text{(A 2)}$$

for $\widetilde{\boldsymbol{w}} = \widetilde{\boldsymbol{w}}^c$ and $\widetilde{\boldsymbol{w}} = \widetilde{\boldsymbol{w}}^s$, where $\boldsymbol{M} = \text{diag}(Pr, -k_\perp^2, -k_\perp^2)$,

$$\boldsymbol{L} = \begin{Bmatrix} -k_\perp^2 & 0 & 0 \\ \widetilde{Ra}/Pr & k_\perp^4 & -\partial_z \\ 0 & -\partial_z k_\perp^2 & k_\perp^4 \end{Bmatrix}, \quad \boldsymbol{N}(\widetilde{\boldsymbol{w}}_{ij}) = \begin{Bmatrix} N_{\theta'} \\ N_\phi \\ N_\psi \end{Bmatrix}, \quad \text{(A 3)}$$

$k_\perp^2 = k_{x,i}^2 + k_{y,j}^2$. In order to avoid spectral convolution, $\boldsymbol{N}$ is derived in physical space as $\boldsymbol{N} = \mathscr{F}\{\boldsymbol{N}_{phys}[\mathscr{F}^{-1}(\widetilde{\boldsymbol{w}})]\}$, where $\mathscr{F}^{-1}$ denotes an inverse DFT, and

$$
\boldsymbol{N}_{phys}(\boldsymbol{w}) = \left\{ \begin{array}{c} Pr[J_\perp(\psi, \theta') + \nabla_\perp^2 \phi \partial_Z \overline{\theta}] \\ J_\perp(\psi, \nabla_\perp^2 \phi) \\ J_\perp(\psi, \nabla_\perp^2 \psi) \end{array} \right\}, \tag{A 4}
$$

where we have suppressed the ij subscripts.

A.2. *Temporal discretization*

As discussed in §3, we employ a mixed implicit/explicit Runge–Kutta scheme developed by Spalart *et al.* (1991). For our system (A 3), the discrete-time equations may be written

$$
[\boldsymbol{L} - (\beta_m \Delta t_n)^{-1} \boldsymbol{M}] \cdot \widetilde{\boldsymbol{w}}_{ij}^{n+m/3} = -\left[\frac{\alpha_m}{\beta_m} \boldsymbol{L} + (\beta_m \Delta t_n)^{-1} \boldsymbol{M} \right] \cdot \widetilde{\boldsymbol{w}}_{ij}^{n+(m-1)/3}
$$
$$
+ \frac{\gamma_m}{\beta_m} \boldsymbol{N}^{n+(m-1)/3} + \frac{\zeta_m}{\beta_m} \boldsymbol{N}^{n+(m-2)/3}, \tag{A 5}
$$

in which three substeps ($m = 1, 2, 3$) constitute a full time step (Δt_n). The step size Δt_n is chosen based on the CFL criterion with respect to the maximum horizontal velocity. For stability, we use $\Delta t_n = 0.68 \Delta_{min} / u_{max}^n$ where Δ_{min} is the minimum grid spacing and u_{max}^n is the magnitude of the maximum horizontal velocity at the end of time step n. For completeness, we give the integration coefficients in (A 5):

$$
\alpha_1 = \tfrac{29}{96}, \quad \alpha_2 = -\tfrac{3}{40}, \quad \alpha_3 = \tfrac{1}{6}, \quad \beta_1 = \tfrac{37}{160}, \quad \beta_2 = \tfrac{5}{24}, \quad \beta_3 = \tfrac{1}{6}, \tag{A 6a}
$$
$$
\gamma_1 = \tfrac{8}{15}, \quad \gamma_2 = \tfrac{5}{12}, \quad \gamma_3 = \tfrac{3}{4}, \quad \zeta_1 = 0, \quad \zeta_2 = -\tfrac{17}{60}, \quad \zeta_3 = -\tfrac{5}{12}. \tag{A 6b}
$$

We rewrite the system as

$$
\theta'^{n+m/3} = \left(k_\perp^2 + \frac{Pr}{\beta_m \Delta t_n} \right)^{-1} \left[\left(-\frac{\alpha_m}{\beta_m} k_\perp^2 + \frac{Pr}{\beta_m \Delta t_n} \right) \theta'^{n+(m-1)/3} \right.
$$
$$
\left. - \frac{\gamma_m}{\beta_m} N_{\theta'}^{n+(m-1)/3} - \frac{\zeta_m}{\beta_m} N_{\theta'}^{n+(m-2)/3} \right], \tag{A 7a}
$$

$$
\partial_Z^2 \phi^{n+m/3} - k_\perp^2 \left(k_\perp^2 + \frac{1}{\beta_m \Delta t_n} \right)^2 \phi^{n+m/3} = k_\perp^2 \left(k_\perp^2 + \frac{1}{\beta_m \Delta t_n} \right) R_\phi + \partial_Z R_\psi, \tag{A 7b}
$$

$$
\partial_Z^2 \psi^{n+m/3} - k_\perp^2 \left(k_\perp^2 + \frac{1}{\beta_m \Delta t_n} \right)^2 \psi^{n+m/3} = k_\perp^2 \partial_Z R_\phi + k_\perp^2 \left(k_\perp^2 + \frac{1}{\beta_m \Delta t_n} \right) R_\psi, \tag{A 7c}
$$

where

$$
R_\phi = \frac{\widetilde{Ra}}{Pr \, k_\perp^2} \theta'^{n+m/3} + \frac{\alpha_m \widetilde{Ra}}{k_\perp^2 \beta_m \, Pr} \theta'^{n+(m-1)/3} - \frac{\alpha_m}{k_\perp^2 \beta_m} \partial_Z \psi^{n+(m-1)/3}
$$
$$
+ \left(\frac{\alpha_m}{\beta_m} k_\perp^2 - \frac{1}{\beta_m \Delta t_n} \right) \phi^{n+(m-1)/3} - \frac{\gamma_m}{k_\perp^2 \beta_m} N_\phi^{n+(m-1)/3} - \frac{\zeta_m}{k_\perp^2 \beta_m} N_\phi^{n+(m-2)/3}, \tag{A 8a}
$$

$$R_\psi = -\frac{\alpha_m}{\beta_m}\partial_Z\phi^{n+(m-1)/3} + \left(\frac{\alpha_m}{\beta_m}k_\perp^2 - \frac{1}{\beta_m\Delta t_n}\right)\psi^{n+(m-1)/3}$$

$$-\frac{\gamma_m}{k_\perp^2\beta_m}N_\psi^{n+(m-1)/3} - \frac{\zeta_m}{k_\perp^2\beta_m}N_\psi^{n+(m-2)/3}, \tag{A 8b}$$

and the subscripts ij have again been suppressed.

A.3. *Vertical spatial discretization*

Finally, we transform Z such that $Z \in [-1, 1]$ and discretize in the vertical with N_Z nodes located at the roots of the Chebyshev polynomial: $Z_k = \cos[(k-1)\pi/(N_Z - 1)]$. With this discretization, we expand dependent variables as

$$\widetilde{\boldsymbol{w}}_{ij}^n(Z) = \sum_{k=0}^{N_Z-1} \widetilde{\boldsymbol{w}}_{ijk}^n T_k(Z), \tag{A 9}$$

where T_k is the kth-order Chebyshev polynomial. Substitution of (A 9) into (A 7), multiplication by $T_l(Z)$ and appropriate weight function (see Gottlieb & Orszag 1977), and integration over $[-1, 1]$ yields a diagonal system for $\theta'^{n+m/3}$ and tridiagonal systems for $\phi^{n+m/3}$ and $\psi^{n+m/3}$ (after some manipulation) that must be solved at each time step. To satisfy boundary conditions, we use tau correction (Gottlieb & Orszag 1977), where the highest two modes are sacrificed to satisfy boundary conditions.

For solution, we first solve (A 7ca) for $\theta'^{n+m/3}$, and apply tau correction to ensure that $\theta'^{n+m/3} = 0$ at upper and lower boundaries. We then solve the remaining two tridiagonal systems for $\phi^{n+m/3}$ and $\psi^{n+m/3}$ subject to boundary conditions (2.30a) and (2.31a), respectively. All fields are de-aliased with the standard 2/3 rule at each time substep.

REFERENCES

BAJAJ, K. M. S., LIU, J., NABERHUIS, B. & AHLERS, G. 1998 Square patterns in Rayleigh–Bénard convection with rotation about a vertical axis. *Phys. Rev. Lett.* **81**, 806–809.

BASSOM, A. P. & ZHANG, K. 1994 Strongly nonlinear convection cells in a rapidly rotating fluid layer. *Geophys. Astrophys. Fluid Dyn.* **76**, 223–238.

BOUBNOV, B. M. & GOLITSYN, G. S. 1986 Experimental study of convective structures in rotating fluids. *J. Fluid Mech.* **167**, 503–531.

BOUBNOV, B. M. & GOLITSYN, G. S. 1995 *Convection in Rotating Fluids*. Kluwer.

CANUTO, V. M. & DUBOVIKOV, M. S. 1998 Two scaling regimes for rotating Rayleigh–Bénard convection. *Phys. Rev. Lett.* **80**, 281–284.

CARTON, X. J. 1992 On the merger of shielded vortices. *Europhys. Lett.* **18**, 697–703.

CHAN, S. K. 1974 Investigation of turbulent convection under a rotational constraint. *J. Fluid Mech.* **64**, 477–506.

CHANDRASEKHAR, S. 1953 The instability of a layer of fluid heated below and subject to Coriolis forces. *Proc. R. Soc. Lond.* A **217**, 306–327.

CHANDRASEKHAR, S. 1961 *Hydrodynamic and Hydromagnetic Stability*. Oxford University Press.

CLUNE, T. & KNOBLOCH, E. 1993 Pattern selection in rotating convection with experimental boundary conditions. *Phys. Rev.* E **47**, 2536–2550.

CONSTANTIN, P., HALLSTROM, C. & PUTKARADZE, V. 1999 Heat transport in rotating convection. *Physica* D **125**, 275–284.

CONSTANTIN, P., HALLSTROM, C. & PUTKARADZE, V. 2001 Logarithmic bounds for infinite Prandtl number rotating convection. *J. Math. Phys.* **42**, 773–783.

COX, S. M. & MATTHEWS, P. C. 2000 Instability of rotating convection. *J. Fluid Mech.* **403**, 153–172.

GOLDSTEIN, H. F., KNOBLOCH, E., MERCADER, I. & NET, M. 1993 Convection in a rotating cylinder. Part 1: Linear theory for moderate Prandtl numbers. *J. Fluid Mech.* **248**, 1421–1450.

GONCHAROV, V. P. & GRYANIK, V. M. 1987 Dynamics of solitary dissipative vortices: vortex lattices and their stability. *Sov. Phys. JETP* **64**, 976–983.

GOTTLIEB, D. & ORSZAG, S. A. 1977 *Numerical Analysis of Spectral Methods: Theory and Applications*. SIAM, Philadelphia, PA.

HART, J. E., KITTELMAN, S. & OHLSEN, D. R. 2002 Mean flow precession and temperature probability density functions in turbulent rotating convection. *Phys. Fluids* **14**, 955–962.

HART, J. E. & OHLSEN, D. R. 1999 On the thermal offset in turbulent rotating convection. *Phys. Fluids* **11**, 2101–2107.

HUBBARD, W. B., BURROWS, A. & LUNINE, J. L. 2000 Theory of giant planets. *Annu. Rev. Astron. Astrophys.* **40**, 103–136.

HUNTER, C. & RIAHI, N. 1975 Nonlinear convection in a rotating fluid. *J. Fluid Mech.* **72**, 433–454.

JULIEN, K. & KNOBLOCH, E. 1998 Strongly nonlinear convection cells in a rapidly rotating fluid layer. *J. Fluid Mech.* **360**, 141–178.

JULIEN, K. & KNOBLOCH, E. 1999 Fully nonlinear three-dimensional convection in a rapidly rotating layer. *Phys. Fluids* **11**, 1469–1483.

JULIEN, K., KNOBLOCH, E., MILLIFF, R. & WERNE, J. 2006 Generalized quasi-geostrophy for spatially anisotropic rotationally constrained flows. *J. Fluid Mech.* (in press).

JULIEN, K., KNOBLOCH, E. & WERNE, J. 1998 A new class of equations for rotationally constrained flow. *Theoret. Comput. Fluid Dyn.* **11**, 251–261.

JULIEN, K., LEGG, S., MCWILLIAMS, J. & WERNE, J. 1996a Hard turbulence in rotating Rayleigh–Bénard convection. *Phys. Rev.* E **53**, 5557–5560.

JULIEN, K., LEGG, S., MCWILLIAMS, J. & WERNE, J. 1996b Rapidly rotating turbulent Rayleigh–Bénard convection. *J. Fluid Mech.* **322**, 243–273.

KERR, R. M. & HERRING, J. R. 2000 Prandtl number dependence of Nusselt number in direct numerical simulations. *J. Fluid Mech.* **419**, 325–344.

KNOBLOCH, E. 1998 Rotating convection: recent developments. *Intl J. Engng Sci.* **36**, 1421–1450.

KOSCHMIEDER, E. L. 1967 On convection on a uniformly heated rotating plane. *Beitr. Phys. Atmos.* **40**, 216–225.

KUO, H. L. 1966 On the dynamics of convective atmospheric vortices. *J. Atmos. Sci.* **23**, 25–42.

KÜPPERS, G. & LORTZ, D. 1969 Transition from laminar convection to thermal turbulence in a rotating fluid layer. *J. Fluid Mech.* **35**, 609–620.

LEGG, S. & MARSHALL, J. 1998 The influence of the ambient flow on the spreading of convected water masses. *J. Marine Res.* **56**, 107–139.

LEVY, M. A. & FERNANDO, H. J. S. 2002 Turbulent thermal convection in a rotating stratified fluid. *J. Fluid Mech.* **467**, 19–40.

LIU, Y. & ECKE, R. E. 1997 Heat transport scaling in turbulent Rayleigh–Bénard convection: effects of rotation and Prandtl number. *Phys. Rev. Lett.* **79**, 2257–2260.

MARSHALL, J. & SCHOTT, F. 1999 Open-ocean convection: observations, theory, and models. *Rev. Geophys.* **37**, 1–64.

NAKAGAWA, Y. & FRENZEN, P. 1955 A theoretical and experimental study of cellular convection in rotating fluids. *Tellus* **7**, 1–21.

NING, L. & ECKE, R. E. 1993 Küppers–Lortz transition at high dimensionless rotation rates in Rayleigh–Bénard convection. *Phys. Rev.* E **47**, R2991–R2994.

PEDLOSKY, J. 1987 *Geophysical Fluid Dynamics*, 2nd edn. Springer.

PRIESTLEY, C. H. B. 1959 *Turbulent Transfer in the Lower Atmosphere*. The University of Chicago Press.

PROCTOR, M. R. E. & GILBERT, A. D. (Ed.) 1994 *Lectures on Solar and Planetary Dynamos*. Cambridge University Press.

PROUDMAN, J. 1916 On the motion of solids in a liquid possessing vorticity. *Proc. R. Soc. Lond.* A **92**, 408–424.

RIAHI, N. 1977 Upper bound for a rotating fluid. *J. Fluid Mech.* **81**, 523–526.

ROSSBY, H. T. 1969 A study of Bénard convection with and without rotation. *J. Fluid Mech.* **36**, 309–337.

SAKAI, S. 1997 The horizontal scale of rotating convection in the geostrophic regime. *J. Fluid Mech.* **333**, 85–95.

SALMON, R. 1998 *Lectures on Geophysical Fluid Dynamics*. Oxford University Press.

SIGGIA, E. D. 1994 High Rayleigh number convection. *Annu. Rev. Fluid Mech.* **26**, 137–168.

SPALART, P. R., MOSER, R. D. & ROGERS, M. M. 1991 Spectral methods for the Navier–Stokes equations with one infinite and two periodic directions. *J. Comput. Phys.* **96**, 297–324.

SULLIVAN, R. D. 1959 A two-cell vortex solution of the Navier–Stokes equations. *J. Aerospace Sci.* **26**, 767–768.

SVESTKA, Z. & HARVEY, H. J. (Ed.) 2000 *Helioseismic Diagnostics of Solar Convection and Activity*. Kluwer.

SWIFT, J. W. 1984 Convection in a rotating fluid layer. In *Fluids and Plasmas: Geometry and Dynamics* (ed. J. Marsden). Contemporary Mathematics, vol. 28, pp. 435–448. American Mathematical Society.

TAYLOR, G. I. 1923 Experiments on the motion of solid bodies in rotating fluids. *Proc. R. Soc. Lond.* A **104**, 213–218.

VERONIS, G. 1968 Large amplitude Bénard convection in a rotating fluid. *J. Fluid Mech.* **31**, 113–139.

VOROBIEFF, P. & ECKE, R. E. 1998 Vortex structure in rotating Rayleigh–Bénard convection. *Physica* D **123**, 153–160.

VOROBIEFF, P. & ECKE, R. E. 2002 Turbulent rotating convection: an experimental study. *J. Fluid Mech.* **458**, 191–218.

ZHONG, F., ECKE, R. E. & STEINBERG, V. 1991 Asymmetric modes and the transition to vortex structures in rotating Rayleigh–Bénard convection. *Phys. Rev. Lett.* **67**, 2473–2476.

ZHONG, F., ECKE, R. & STEINBERG, V. 1993 Rotating Rayleigh–Bénard convection: asymmetric modes and vortex states. *J. Fluid Mech.* **249**, 135–159.